

<p style="text-align: center;"><b>University of Birmingham</b></p> <p style="text-align: center;">School of Engineering <b>Department of Mechanical Engineering</b></p> <p style="text-align: center;"><b>Individual Engineering Project</b> <b>FINAL REPORT</b></p> <p style="text-align: center;"><b>MEng</b></p>	
Surname	Dawes
First Name(s)	Alexander Keith
ID number	2206650
Supervisor's Name	Professor Khamis Essa
Project Title	Utilisation of neural networks to predict the compressive mechanical properties of TPMS gyroid lattice structures manufactured via laser powder bed fusion

## 1 Table of Nomenclature

<b>NN</b>	Neural Network
<b>ANN</b>	Artificial Neural Network
<b>SNN</b>	Shallow Neural Network
<b>DNN</b>	Deep Neural Network
<b>CNN</b>	Convolutional Neural Network
<b>TPMS</b>	Triply-periodic-minimal-surface
<b>CAD</b>	Computer Aided design
<b>LPBF</b>	Laser Powder Bed fusion
<b>ML</b>	Machine Learning
<b>YM</b>	Young's Modulus
<b>YS</b>	Yield Strength
<b>PTSP</b>	Process-Thermal-Structure-Property
<b>SAE</b>	Stacked Autoencoder
<b>GLWPT</b>	Greedy Layer-wise Pre training
<b>RandWB</b>	Randomised Weights and Biases
<b>MSE</b>	Mean squared error
<b>RMSE</b>	Root mean squared error
<b>SEM</b>	Scanning Electron Microscopy
<b>OP-S</b>	Colloidal silica suspension
<b>Ra</b>	Mean surface roughness

## Contents

<b>1 Table of Nomenclature</b>	1
<b>2 Abstract</b>	3
<b>3 Introduction</b>	3
<b>4 Methodology</b>	4
4.1 Identification of Process and design parameters (Inputs and outputs of NN)	4
4.2 TPMS Network Gyroid	4
4.3 TPMS Sheet Gyroid	4
4.4 Laser Powder Bed Fusion and the Process Thermal Structure Property Relationship	5
4.5 Material	6
4.6 Neural networks	7
4.6.1 Stacked Autoencoder pre-training	8
4.6.2 Greedy Layer wise pre-training	8
4.7 Application of Neural networks on the PTSP relationship for LPBF	8
4.7.1 Process Optimisation and Target Lattices	9
<b>5 Results</b>	9
5.1 Training of Neural Networks	9
5.1.1 Network Gyroid NN Training Plots	10
5.1.2 Sheet Gyroid NN Training Plots	11
5.2 Performance of Neural networks	12
5.3 Validation Set Prediction Performance	13
5.4 Mechanical Testing of LPBF Fabricated TPMS Gyroid Lattices	14
5.4.1 Deformation Mechanisms	14
5.4.2 Target TPMS Sheet Gyroid	14
5.4.3 Target TPMS Network Gyroid	15
5.5 Microscopy	16
5.5.1 SEM Imagery	16
5.5.2 Alicona Optical microscope imagery	17
<b>6 Discussion</b>	18
6.1 Neural Networks, pre-training, and the effects of training iteration 2	18
6.2 Micro-trends	18
6.3 Differences in the PTSP relationship of sheet and network gyroids	19
6.4 Differences observed between modulus and yield strength	19
6.5 ANN Limitations	20
<b>7 Conclusions</b>	20
<b>8 Appendices</b>	21
8.1 Appendix A: NN Training Data	21
8.2 Appendix B: Target lattice process maps	23
8.3 Appendix C: Error histograms for Iteration 2 best networks	25
8.4 Appendix D: Iteration 1 best performing NN validation plots	25
8.5 Appendix E: Supplementary lattice testing results	26
<b>9 Declaration of competing interest</b>	27
<b>10 Acknowledgements</b>	27
<b>11 References</b>	27

## 2 Abstract

TPMS gyroid lattices are mathematically defined lattice structures capable of reducing the bulk properties of the parent material. When manufactured via LPBF, the mechanical properties of these lattices are heavily dependent on the process parameters, the process physics, and the design parameters of the lattices. Therefore, a key task in process optimisation of LPBF for these lattices is to determine a methodology to predict the mechanical properties, so that target application such as bone implants with tailored properties can be realised. In this work, neural networks and pre training are used, operating on a small data set gathered from literature. This data set was improved with lattices manufactured in this study. The best neural networks were used to select the required design and process parameters for gyroid lattices to achieve specific mechanical properties. It was found that Yield strength was more readily predicted and targeted than Young's modulus, and that accuracy of predictions improved with a larger data set. There are also limitations on the surface qualities of the targeted lattices, as the neural network does not consider this when targeting modulus or yield strength.

## 3 Introduction

Laser powder bed fusion (LPBF) has seen an increased use in many industries, such as aerospace and biomedical [1]. LPBF is the process of selectively melting layers of a powder bed together using a laser source, fusing the powder together [2]. With this technology, parts with micro-scale internal features challenging to create with conventional manufacturing methods can be fabricated. Such as lattice structures that can provide high specific mechanical, electrical and thermal properties [3]. Periodic lattice structures are defined as an interconnected network of struts or plates with a repeating unit cell architecture, which introduces porosity into the material. A non-periodic lattice is referred to as stochastic. Due to the introduced porosity, lattice structures have reduced mechanical properties from the parent material [4].

A commonly studied lattice type is the class of triply periodic minimal surface (TPMS) lattices. These are mathematically defined geometries with zero mean curvature in all 3 cartesian directions. Resulting in continuous surfaces with no sharp edges, which eliminates stress concentrations thereby improving mechanical performance compared to strut-based lattices [5]. From the TPMS category, the sheet and network gyroid lattices have promising applications due to their manufacturability and biocompatibility [6]. These traits arise from the highly curved unit cell architecture, which enables 3-D printing with no internal supports, at wall thicknesses of less than 200 microns [5]. This provides the potential for excellent mass transport, cell-attachment, and cell-proliferation [7]. As such, these lattices have seen significant interest in biomedical implants.

Ti-6Al-4V has seen significant use in bone implants due to its exceptional biocompatibility [8]. However, the bulk property of young's modulus is significantly higher than human bone, which can lead to stress shielding in implants [7]. TPMS lattices can be used to reduce the modulus of Ti-6Al-4V to a suitable value. However, the mechanical properties of a lattice structure fabricated via LPBF are hard to determine in advance [9]. Predicting the mechanical properties requires a method of interpreting the process thermal structure property relationship (PTSP) [10]. Pertaining to the link between; process parameters, thermal multi-physics, the geometry/structure of the lattice, to the resulting mechanical properties. Lattice structures with reliable mechanical properties would be useful in many engineering applications [11]. Previous works have attempted to simplify the PTSP relationship by only considering the design of the lattice, omitting process parameters [12],[13]. [14] implemented custom Johnson-cook parameters in a finite element analysis investigation of sheet and network gyroids.

Due to the highly non-linear nature of this PTSP relationship [15] a key research area in process optimisation has been the use of data driven machine learning (ML) solutions [9]. Within ML, Deep Neural Networks (DNN) have been shown to have promising performance in regression tasks for non-linear systems [16]. However, DNN's require significant data set sizes to achieve this performance [17]. This is not something that is readily available in the field of LPBF of lattice structures due to low throughput as well as various

constraints that limit the availability of consistent data. However, the performance of DNN on small data sets can be improved with pre-training [16].

Hence, in this study, key process parameters of LPBF, alongside lattice design parameters, were used by Neural Networks (NN) to predict and target the mechanical properties of Ti-6Al-4V TPMS network and sheet gyroid lattice structures. This was achieved with data collected from previous studies in the relevant literature.

## 4 Methodology

### 4.1 Identification of Process and design parameters (Inputs and outputs of NN)

The process parameters of laser power (P), scanning speed (V) and hatch spacing (H) and layer thickness (T) were identified as the most important process parameters that are consistently referenced[18]. These can also be combined in equation 1, volumetric energy density ( $\rho$ ). These were the process parameters used as NN inputs.

$$\rho = \frac{P}{VHT} \quad \text{Equation 1}$$

For the mechanical response, corresponding to the outputs of the NN's, the young's modulus (YM) and yield strength (YS) in compression were selected. Being the most consistently referenced as they are needed for many applications of TPMS lattices, such as avoiding stress shielding in biomedical implants[19], and energy absorption applications [20].

The two lattices being investigated are the TPMS network gyroid, and TMPS sheet gyroid. Their smooth surfaces make them excellent for 3-D printing [5]. Specifically, the sheet and network gyroids have seen prevalent study due to their excellent mechanical properties when compared to other TPMS lattices [21]

### 4.2 TPMS Network Gyroid

The network gyroid is defined by equation 2 [14].

$$NG(x, y, z) = \sin\left(\frac{2\pi x}{L}\right) * \cos\left(\frac{2\pi y}{L}\right) + \sin\left(\frac{2\pi y}{L}\right) * \cos\left(\frac{2\pi z}{L}\right) + \sin\left(\frac{2\pi z}{L}\right) * \cos\left(\frac{2\pi x}{L}\right) \leq t^2 \quad \text{Equation 2}$$

### 4.3 TPMS Sheet Gyroid

The sheet gyroid is produced as a subtraction of two network phases [14]. A matrix phase with an arbitrary volume fraction can be specified as the volume between two isosurfaces generated by  $NG(x, y, z) = 0$ .

Therefore, the implicit function for a sheet gyroid is shown in equation 3:

$$SG(x, y, z) = [NG(x, y, z)]^2 - t^2 \quad \text{Equation 3}$$

Where the void domain is the positive region,  $SG \geq 0$ , the negative region the solid domain,  $SG \leq 0$ . Figure 1 showcases the different structures of the gyroid types.

The equation 2 parameters, L and t can be varied to produce lattices with specific cell sizes and relative densities respectively. Due to the consistent geometry defined by the equations, the gyroid lattices can be uniquely defined by the relative density and the unit cell size [21]. This lattice design procedure reduces the number of design parameters compared to a strut-based lattice with more factors, such as strut inclination angle [12]. This simplicity makes collecting data between different studies consistent, proving advantageous for increasing data set size. Relative density and unit cell size were used as inputs to the NN's. The training data set can be found in Appendix A.

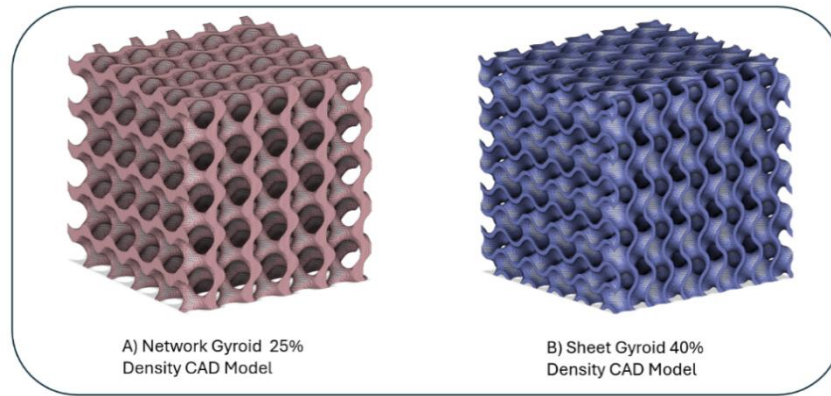


Figure 1- CAD models of the two TPMS Gyroid Lattices.

#### 4.4 Laser Powder Bed Fusion and the Process Thermal Structure Property Relationship

PTSP is often interchangeable with terms such as melt pool or multi-physics [10]. In this work, the PTSP was thought of as an unknown non-linear function of many variables, constituting the process and design parameters, the underlying physics of the system and function output being the mechanical properties. This function was approximated with the process and design parameters.

Previous works [22],[23],[12], have looked at predicting the mechanical properties of lattice structures using ML methods, but focus on the structure-property relationship, and a gap was identified specifically on the PTSP of TPMS gyroid lattices. This study furthered these approaches by incorporating the process parameters.

To aid the NN training, separate data sets were made for each gyroid type. A set for sheet gyroids (41 data points), and a set for network gyroids (34 data points). As the different lattices have different PTSP relationships [10]. The inputs to the NN's were normalized between 0 and 1.

The ground truths for training the NN's (Mechanical properties) were normalized with respect to the parent material (Ti-6Al-4V) bulk properties for young's modulus (YM) and yield strength (YS).

The data in each set was randomly divided into training (80%) and validation (20%) sets. Training indices were kept identical across the NN being compared for each lattice; for fair comparisons of the NN performance, as it was found that the data division can alter the solution achieved.

Within the data gathered from literature there were gaps in the energy densities recorded. Energy density was used to simplify the 4-dimensional space of processing parameters into 1 variable. Although [24] highlights the issues with  $\rho$ , this simplification was afforded. Therefore, in this work additional lattices, Figure 2, were printed using a RenAM500S out of Ti-6Al-4V powder. Eight cubic samples were printed with total dimensions 15x15x15 mm, and were subject to mechanical compressive testing, using a strain rate of  $10^{-2}$ s according to ISO 13314–2011, using an Instron 34TM-30 and Avery 60T load frame. These were used to supplement the data from literature by attempting to fill the gaps in energy density for both gyroid types, table 1. Therefore, there were two training Iterations, Iteration 1 with only literature data. Iteration 2 with the literature and supplementary data. All lattices in this study were designed using [25].

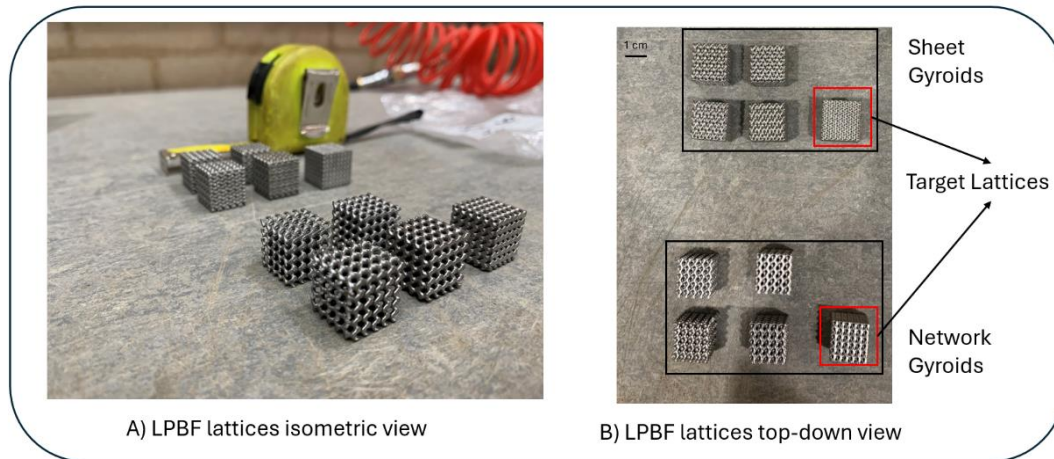
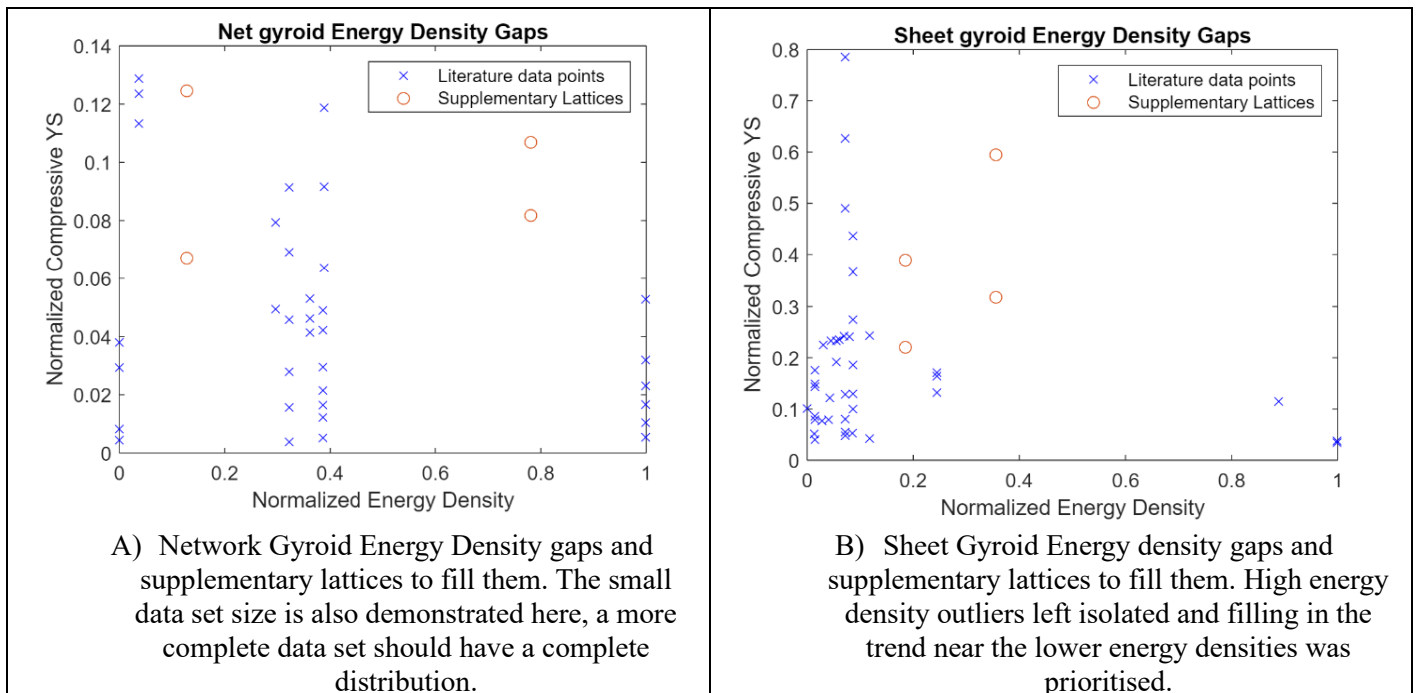


Figure 2 -Isometric and top-down views of the TPMS lattices printed by LPBF in this work. Highlighted are the target lattices used for compressive testing. There were an additional two copies of the Target lattices that were printed and used for microscopic evaluation of print surface quality.

Table 1 -Plots highlighting the gaps in energy density that were present in the TPMS lattice data sets from literature data.



#### 4.5 Material

The material chosen was Ti-6AL-4V, due to its prevalent use in biomedical implants enhancing data availability. In LPBF, the material must be atomised into a powder, and differences in the powder cause differences in the PTSP behaviour [26]. This work does not characterise the powder variation and assumes it is constant across all data sources. The powder used to fabricate the samples in this study was sourced from Advanced Powders and Coatings- a GE company. This Powder is spherically atomised. Grade 23, Ti-6AL-4V, low interstitial powder, with a 15–45-micron particle size range.

#### 4.6 Neural networks

The NN, is a type of function fitting ML method composed of input, hidden and output layers, inspired by the human brain that makes use of tuneable parameters known as weights and biases [27]. These weights and biases are stored in individual neurons in hidden layers and are altered via a training algorithm to capture the trends seen in data. The generic structure of the most basic NN, the shallow NN (SNN) with a single hidden layer, and the structure of an individual neuron in the hidden layer is depicted in Figure 3.

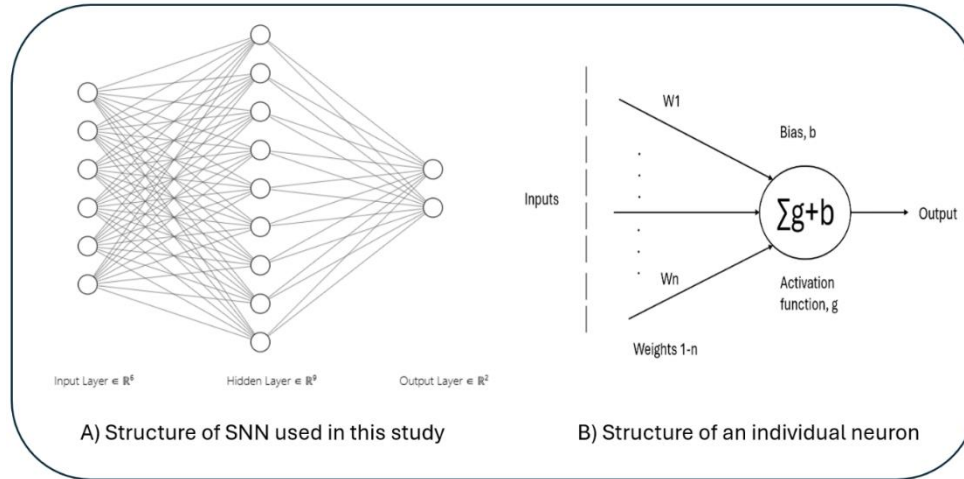


Figure 3- Structure of a Fully connected SNN and the constituent individual hidden layer neuron, with activation function ( $G$ ), and weights ( $W$ ), Bias ( $b$ ).

The hidden layers consist of neurons which consist of a weight, activation function and a bias. The weight multiplies the incoming input. The activation function transforms this multiplied value. All the NN architectures used in this study incorporate the Tanh activation function (Equation 4) [28].

$$n = \frac{2}{(1 + e^{-2n}) - 1} \quad \text{Equation 4}$$

Then the bias is added to the value before being passed to the subsequent neuron. Finally, the output layer displays the predicted output, which is a continuous variable in regression. Training algorithms minimise the difference between the predicted and actual response for the outputs on the training data. Resilient back propagation was used in this work, on MATLAB, 2024b [29]. Through the addition of more hidden layers and more neurons increasingly complex relationships can be approximated, although overfitting must be avoided [27]. A SNN consists of a single hidden layer. A DNN consists of three or more hidden layers [12]. Typically, large data sets are needed to train a DNN, on the order of 10,000 data points. However, this study used pre-training methods. Pre-training attempts to initialize the weights and biases in the network to values that avoid any local optimal solutions [16], and hence can be used to avoid overfitting, improve training speed, and reduce the need for large data sets.



#### 4.6.1 Stacked Autoencoder pre-training

The stacked auto-encoder (SAE) method uses a type of NN known as an autoencoder. An autoencoder consists of an input layer, a hidden layer, and an output layer with the same number of nodes as the input layer. The autoencoder attempts to re-create the input in its output [30]. Stacked auto-encoder pre-training uses a sequence of autoencoders to find optimal initial weights and biases for the main NN [16]. The first autoencoder has the same number of neurons in the hidden layer as the input layer of the main NN and takes the normalized input data as its input. After training, the weights and biases of the hidden layer are copied to the input layer of the main network and the transformed output of the hidden layer is taken as the input to the second autoencoder. This second autoencoder has the same number of neurons as the first hidden layer of the main network. This is then trained, and the weights and biases of the hidden layer are copied to the first hidden layer of the main network. Then the transformed output is sent to the third autoencoder. This process is repeated until all the neurons of the main network have had their weights and biases initialised, after which regular training ensues. For the SAE pre-training used in this study, the SAE sequence had the following structure (6-9-6) (9-9-9) (9-9-9) (9-2-9). This process is summarised in Figure 4. [16] previously used the SAE method to enhance the performance of a DNN on a small data set.

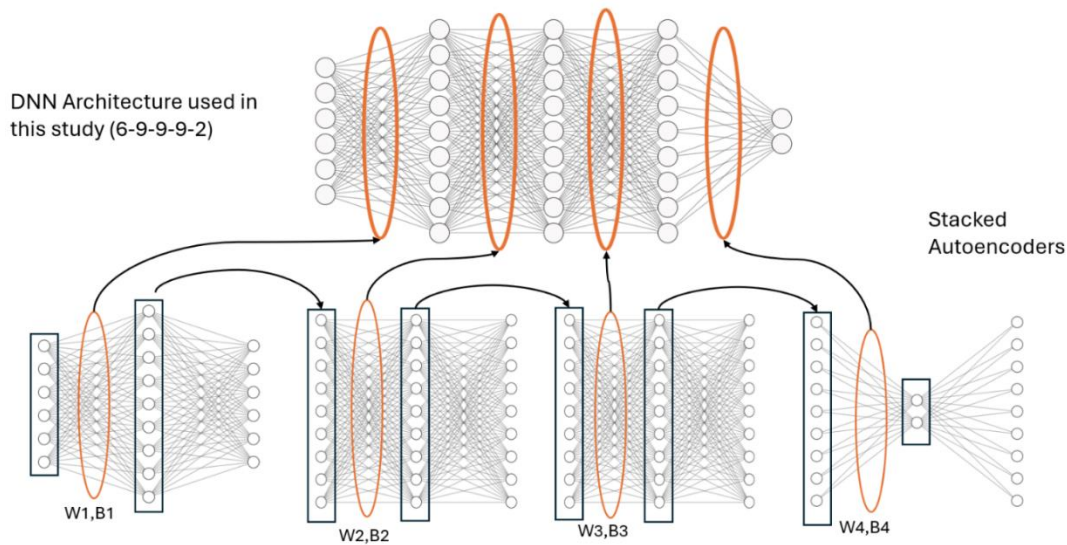


Figure 4- Diagram of the Stacked autoencoder method used in this study.  $W$  and  $B$  represent the weights and biases being transferred from the autoencoders to the main DNN. Arrows denote the direction of information transfer.

#### 4.6.2 Greedy Layer wise pre-training

Greedy layer wise pre-training (GLWPT) builds on the SAE approach, by initialising the network with the SAE weights and bias values. Then training each individual layer separately, but in sequence. This aims to allow for features in the data to be identified by the initial layer, and then subsequent layers to operate on these features. This aims to perceive more detailed trends in the data. [12] used greedy layer wise pre-training in the training procedure for a similar NN task of predicting the mechanical properties of diamond strut-based lattice structures.

#### 4.7 Application of Neural networks on the PTSP relationship for LPBF

For both TPMS lattice data sets in this work, a SNN consisting of a single hidden layer, and three DNN were trained. One using SAE, another with GLWPT and another with randomised initial weights and biases. Corresponding to the standard initialisation procedure and will be referred to as RandWB. The architecture of the DNN's trained was kept the same and is shown in Figure 4. The SNNs used a single layer, Figure 3-A. The NN's were compared using the RMSE regression metric on the validation data.



#### 4.7.1 Process Optimisation and Target Lattices

The best networks from Iteration 1 were used in an objective function to design two lattices with targeted mechanical properties. Based on machine constraints, the hatch spacing, and the layer thickness had to be fixed at 90 and 30 microns respectively. Therefore, the NN could only alter both lattice design parameters, laser power and scan speed to target the properties. The target properties were specified by the potential application of these lattices to human bone which has a range of YM from 3-30 GPa [31]. Both extremes of the YM were targeted. The target YS was not specified to avoid configuring the ratio of the two mechanical properties into impossible values. However, the NN prediction for the expected YS of these target lattices was evaluated. The design and process parameters that the NN's provided can be found in Table 2. Two of each target lattice were made, one pair for compressive testing, the other for microscopic investigation.

*Table 2-Target lattice process and design parameters supplied by best performers from Iteration 1 (SAENET and RWBSHEET)*

Lattice	Target YM (MPa)	Laser Power (W)	Scan Speed (mm/s)	Hatch Spacing (mm)	Layer Thickness (mm)	Relative Density (%)	Unit Cell size(mm)	Dimension (mm)
Target Network	3000	350	970	0.09	0.03	46	2.5	15x15x15
Target Sheet	25000	205	700	0.09	0.03	62	2	16x16x16

Process maps of laser power and scan speed were also generated based on the lattice design constraints and machine constraints. These provide a good visualisation of the trends the NN identifies. (Appendix B)

## 5 Results

### 5.1 Training of Neural Networks

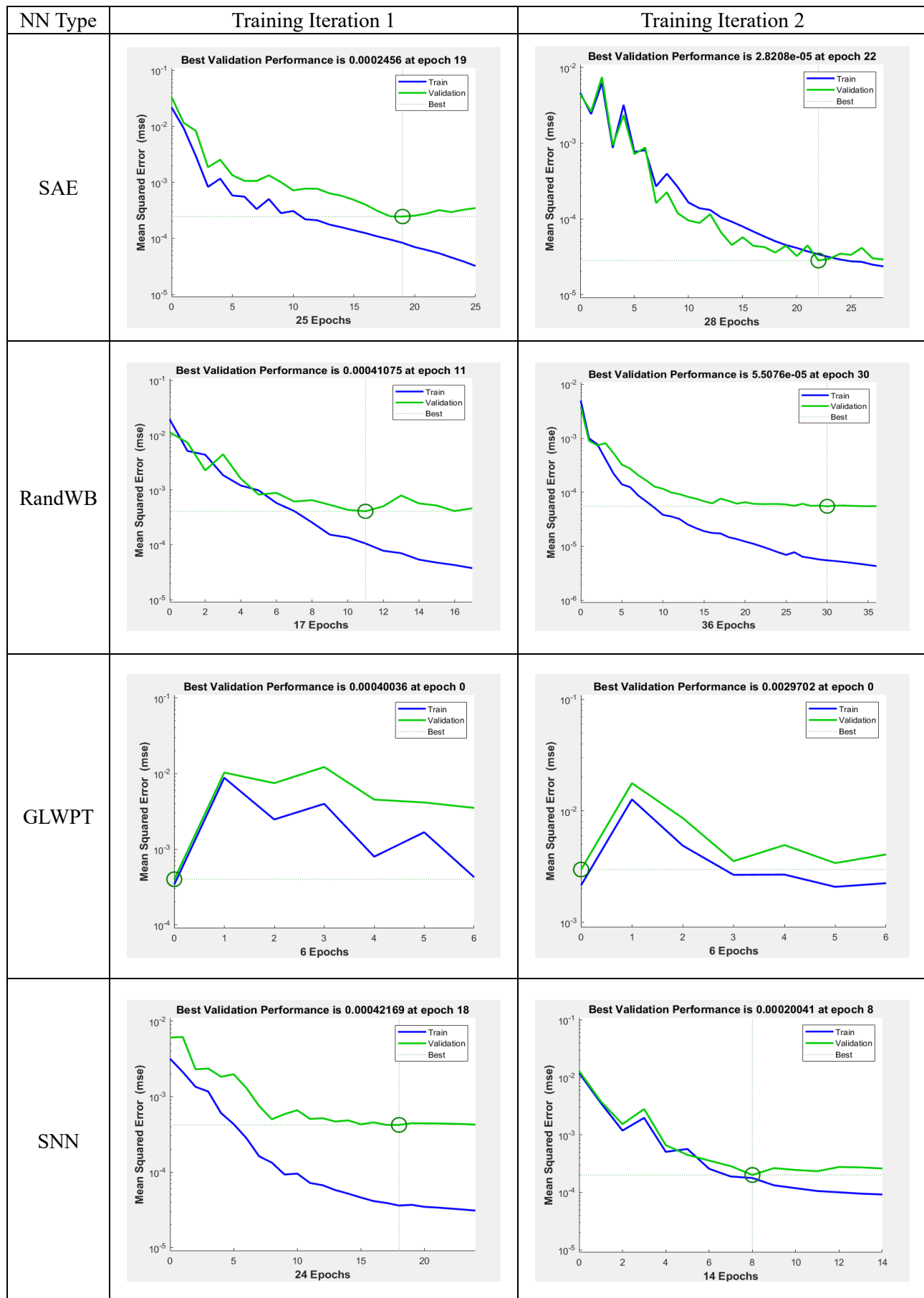
The training plots and the RMSE values were used to evaluate the differences between the NN training procedures. The best performing NN from both training iterations were evaluated in more detail, by investigating the specific performance on the data points within the validation data and the target lattices. The primary observation in the training is the lack of consistency, due to the small data set size. The division of data plays changes the quality of the solution, and different training runs will produce differing results. For this reason, the results presented are the best for each category of NN observed after numerous runs. And the comparison of different NN is done with the same data division.

The training plots, tables 3 and 4, showcase that the SNN offers a reasonable solution with no pre-training. The RandWB and SAE method train for a larger number of epochs, as there are more complex patterns in the data that these networks can identify, that the SNN cannot. For both lattices, the GLWPT has the largest errors, and overfitting can be seen as validation and training data diverge with more epochs of training. The initial value of error for the GLWPT shows that the pre-training method has initialised the weights and biases in a local solution, with a reduced MSE. However, this MSE is only comparable to the performance of the SNN, even though the GLWPT has a DNN architecture.

For the network gyroid SAE in iteration 2, the initial reduced MSE demonstrates the benefits of the pre-training method. Without demonstrating overfitting as validation and training data remain similar. This NN also has the lowest RMSE. The network gyroid NN's train for a greater number of epochs than the Sheet gyroid NN's and reach lower values of error for both training and validation.

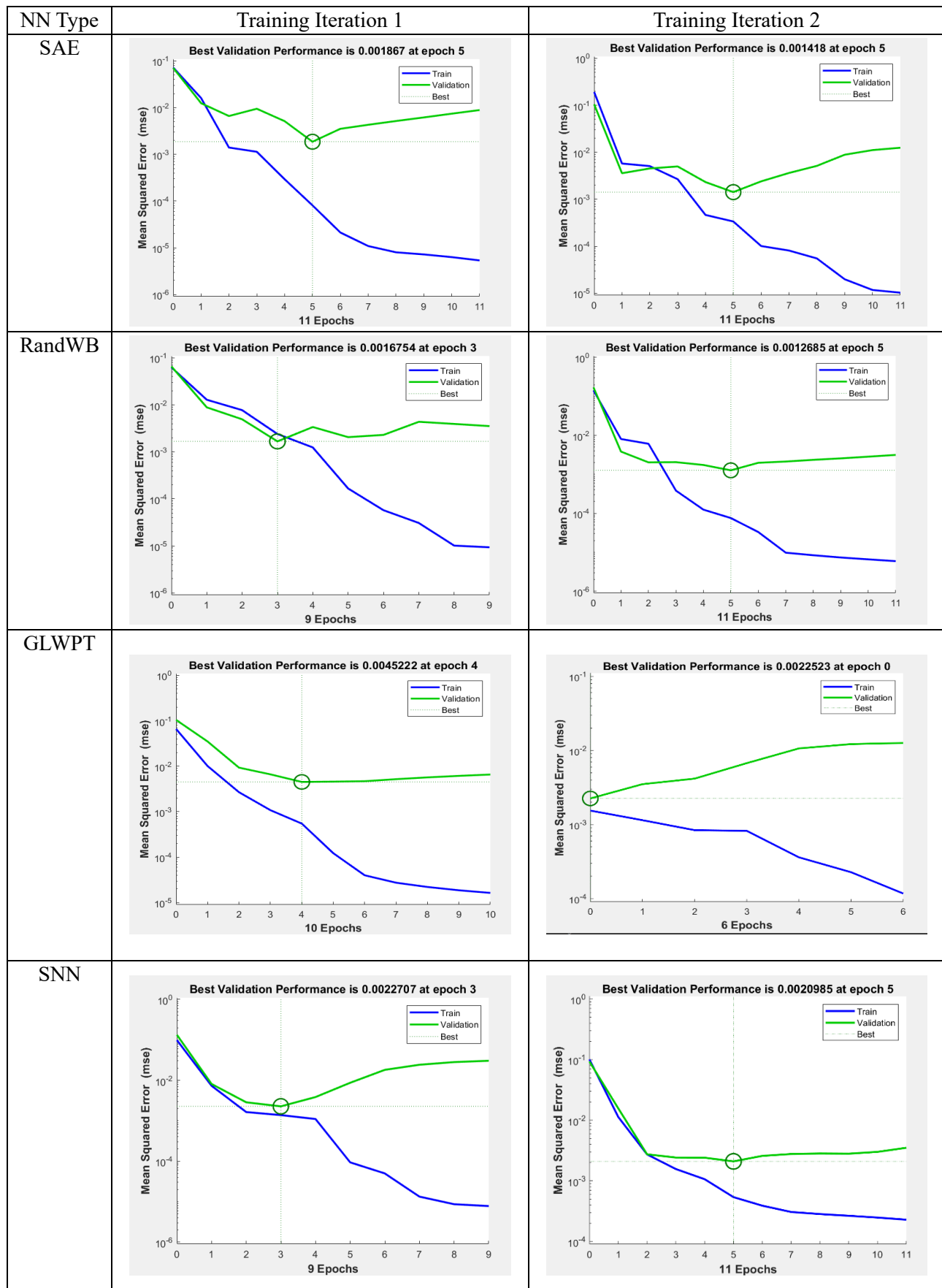
## 5.1.1 Network Gyroid NN Training Plots

Table 3-Network gyroid NN training plots comparison of different training strategies and SNN.



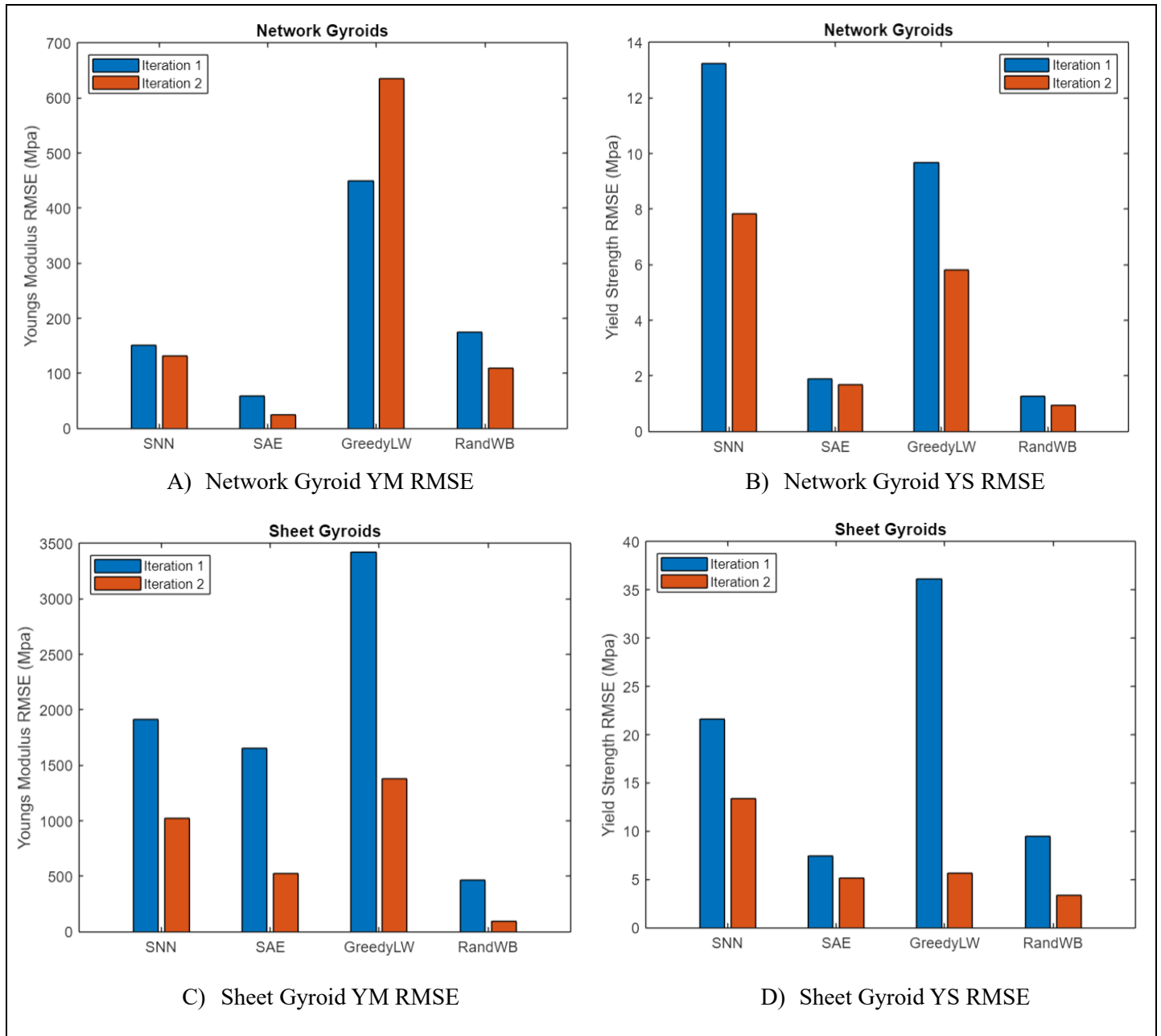
## 5.1.2 Sheet Gyroid NN Training Plots

Table 4- Sheet gyroid NN training plots comparison of different training strategies and SNN.



## 5.2 Performance of Neural networks

Table 5- RMSE plots of all the NN training strategies compared in this study, across both iterations.



It can be seen in table 5, that with the addition of the additional training data inside the energy density gaps identified, the RMSE decreases for both YM and YS in all the NN's, except the network gyroid GLWPT YM prediction, which increases.

The additional data does not change which NN is the best performing for each lattice, as all NN's receive the additional data. The NN's for the network gyroids have lower RMSE in both properties, than the sheet gyroid NN's. Therefore, the network gyroid's mechanical properties are more accurately predicted than a sheet based gyroid, for a similar data set size. To note there is also inconsistency in the GLWPT performance. As it reduces RMSE after Iteration 2 in the sheet gyroid but increases RMSE in the network gyroid.

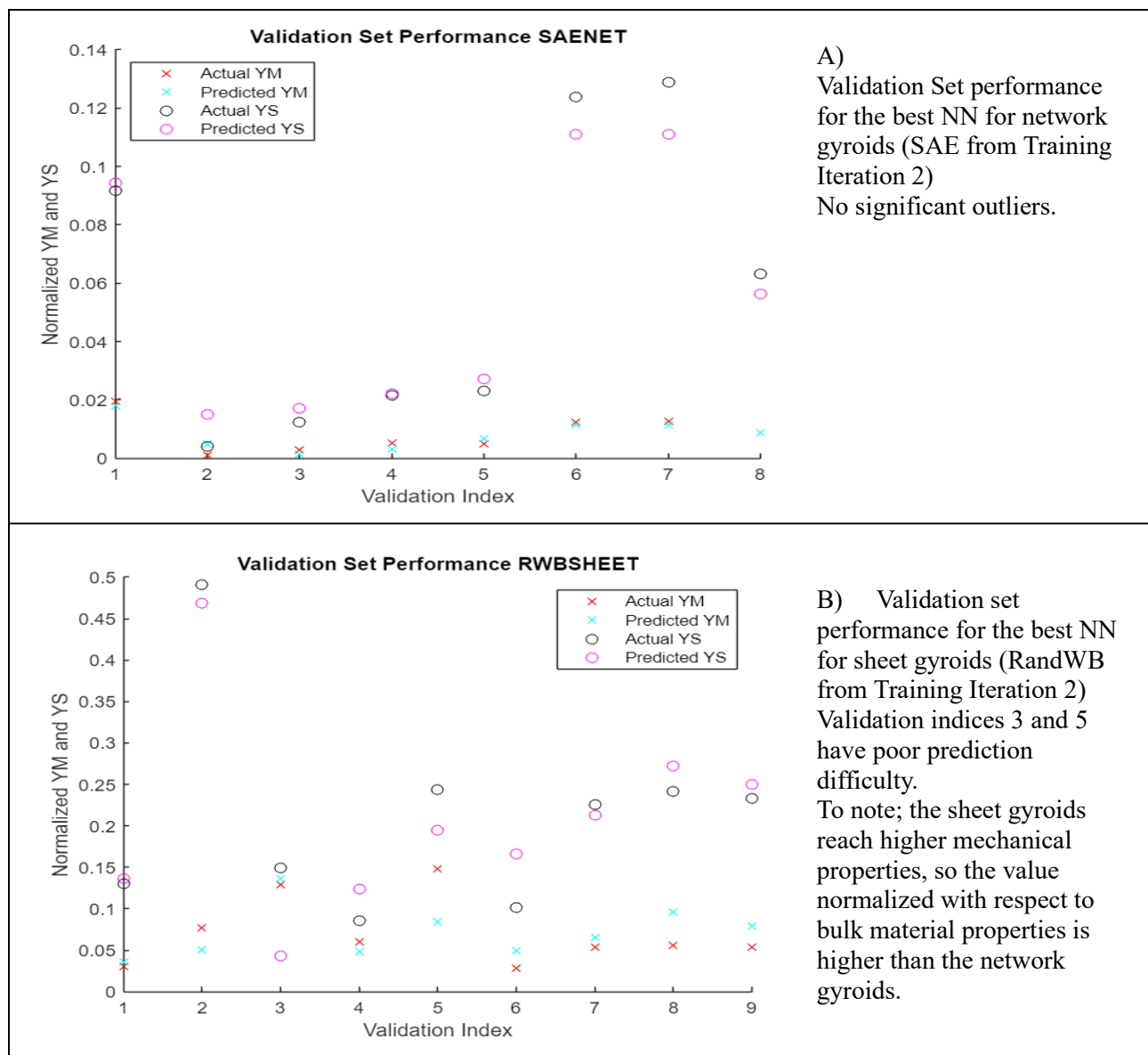
YS observes significantly lower RMSE values in all NN's for both lattices compared to YM. Therefore, YM is a more complex parameter that is harder to predict.

After Iteration 1, the two networks that were selected to ‘design’ the target lattices were the SAE for the network gyroids, and the RandWB for the sheet gyroids. Which had the lowest combined RMSE in their respective lattice categories. These networks both improved and remained the best performing after Iteration 2; with SAE for the network gyroids achieving a combined RMSE of 26.88 MPa. Whilst the RandWB for sheet gyroids achieved a combined RMSE of 100.15 MPa.

### 5.3 Validation Set Prediction Performance

There is a more variation between the predicted and actual values of the validation set for the sheet gyroid than the network gyroid, table 6. Appendix C, containing error histograms shows the larger normalized error for sheet gyroids. SAE demonstrates more consistent prediction accuracy of the validation set for network gyroids than the RandWB does for sheet gyroids, with no outlying points. Most RandWB values are approximated well, certain data points such as, table 6-B Validation index 3 and 5, have increased error. These data points do not correspond to the approximated function the network has identified. Therefore, more data points are needed to approximate the PTSP globally. There is similar normalized performance between YM and YS for both NN, but due to the scale of these properties, YM has higher error values. Appendix D also shows the corresponding validation plots for Iteration 1 of these networks.

Table 6- Validation Set prediction vs actual value plots for the Best performing NN from Iteration 2



#### 5.4 Mechanical Testing of LPBF Fabricated TPMS Gyroid Lattices

Stress-strain graphs for the supplementary lattices can be found in Appendix E. It was found that the increased energy density, with the same design parameters, generally increased both the YM and YS of the lattice. With the notable opposite of Net 35 gyroid reducing in both YM and YS with increased energy density. Demonstrating the PTSP non-linearity. Network gyroids encountered the yield strength at 6-8% strain, whilst Sheet gyroids yielded at 11-15 % strain. The network gyroids have reduced mechanical properties compared to sheet gyroids, for higher relative densities, in agreement with [7],[6].

##### 5.4.1 Deformation Mechanisms

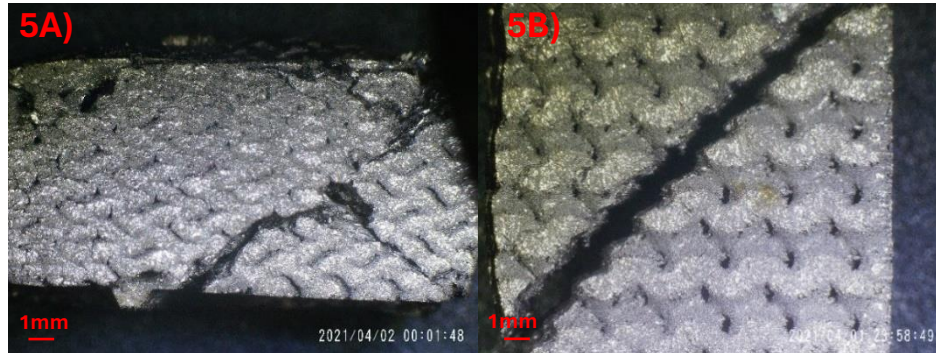


Figure 5A) Target Sheet Gyroid after compressive test, ~60% strain. 5B) Target network gyroid after compressive mechanical test, shear failure at ~21% strain.

The network gyroids undergo layer by layer failure[14], constituting layer collapse with subsequent densification [32]. Shown by regions of strain hardening followed by drops where the layer collapses, seen in Figure 7. This behaviour pre-empted shear failure along the diagonal, which splits the lattice into two halves, Figure 5-B. This happened after the third round of densification.

The sheet gyroid observes simultaneous collapse of all the layers. In agreement with results of continuously graded results in literature with this lattice type [33][34][35]. At high levels of strain ~60%, the gyroid begins to exhibit shear cracking as seen in Figure 5-A, occurring after densification as the layers become totally compressed [4]. The location of the formed shear band was off centre, and split the lattice into several pieces, resulting in brittle failure.

##### 5.4.2 Target TPMS Sheet Gyroid

The Target sheet gyroid exhibits a consistent elastic region, and the yield point can be easily identified, Figure 6. The plastic region exhibits additional strain hardening at 35% strain where the layers fail simultaneously and begin to press into each other (densification). As the target lattice had a relative density of 62% this highlights the link between the selected relative density and the onset of a secondary period of strain hardening. This link has potential application in energy absorption applications [36].

There was significant deviation from the target modulus and the actual modulus, table 7. Although with Iteration 2, the modulus prediction is reduced significantly to within 25.39% of the actual value. The YS prediction has better accuracy in both iterations and improves to within 3.51% in Iteration 2.

Table 7- Summary of predictions and actual values for the target sheet gyroid lattice

Target Sheet	Target (MPa)	Iteration 1 Prediction (MPa)	Iteration 2 Prediction (MPa)	Actual Value (MPa)	% Accuracy
Youngs Modulus	25000	24838	6989.1	5214.9	25.39%
Yield Strength	NA	712	632.1	609.9	3.51%

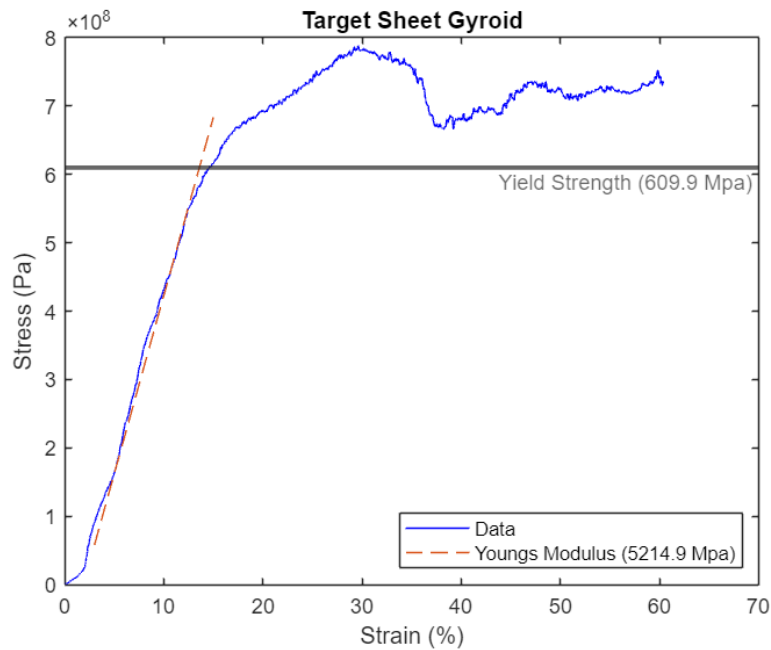


Figure 6- Stress Strain curve for the Target Sheet Gyroid

#### 5.4.3 Target TPMS Network Gyroid

The yield strength of the target network gyroid precedes a strain hardening region, Figure 7, without a significant drop in the modulus from the elastic region. The yield point was difficult to identify because of this. But was chosen due to the strain (8%) consistent with the yield point of the other network gyroids tested. Plastic behaviour denoted by the curve present in the region after the selected point, the offset of the curve to the right, and due to an audible ‘crack’ that occurred at this point in the compressive test. The layer-by-layer failure and layer densification can be seen, typical behaviour for stretch dominated lattices [4][37].

In table 8, the target and actual value for YM differed, and both training Iterations under predict the YM, with minimal variation between iterations, only achieving 31.8 % accuracy. The YS observed better accuracy, and is improved by the second iteration of training, to within 8.76 %.

Table 8- Summary of predictions and actual values for the target network gyroid lattice

Target Network	Target (MPa)	Iteration 1 Prediction (MPa)	Iteration 2 Prediction (MPa)	Actual Value (MPa)	% Accuracy
Youngs Modulus	3000	2872	2930.6	4297.1	31.8%
Yield Strength	NA	193.8	125.6	137.67	8.76%

Overall, the target lattice property prediction behaves similarly to the validation data behaviour. With a much-improved YS prediction compared to YM. Although similar levels of accuracy were observed for both gyroid types.



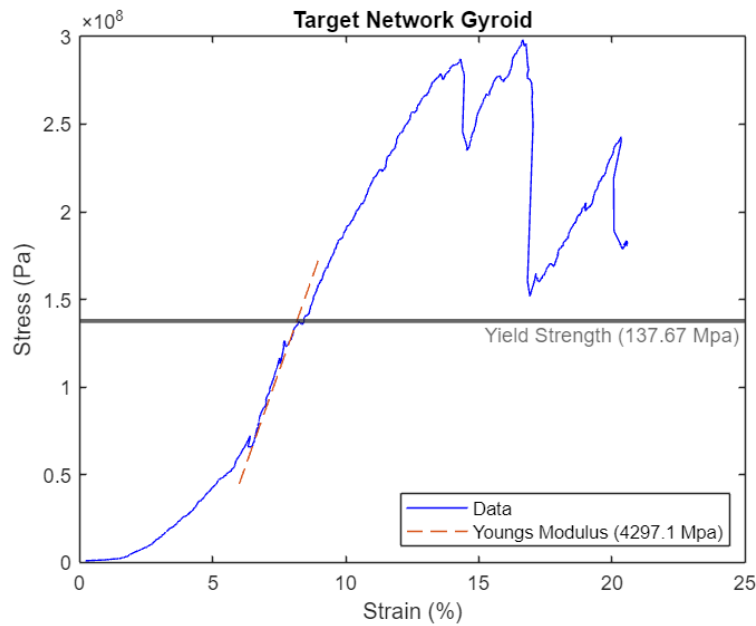


Figure 7- Stress Strain Curve for the Target Network Gyroid

### 5.5 Microscopy

Prior to the mechanical testing, all lattices were subjected to an ultrasonic bath (Ultra wave), in a 5% by volume ethanol and water mixture to remove trapped powder. Ultrasonic treatment does not affect the mechanical properties [38]. However, the microscopy still showed significant powder on the surfaces of the target lattices, especially the internal surfaces and sides parallel with the build direction. This LPBF defect is known as balling [39][40]. Although the surface roughness may cause enhanced bone integration [41], there is significant potential for the half adhered spherical powders to become loose during implant loading. This could result in wear debris in the size range to cause osteolysis [42].

#### 5.5.1 SEM Imagery

The SEM images, Figures 8 and 9, were taken using JOEL 6000. Samples were mounted in buckalite, before being polished using Struers Tegramin-25 with OP-S suspension. The buckalite did not manage to penetrate the target sheet gyroid pores, due to their smaller size. Allowing for some vision of the internal surfaces where large amounts of adhered powder could be seen.

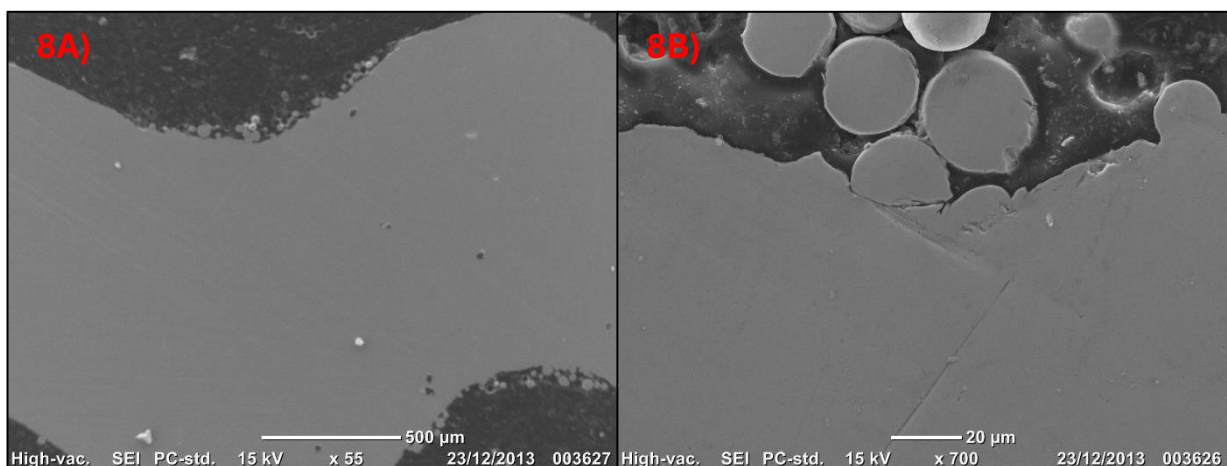


Figure 8- Target Network gyroid SEM images, small scale porosities 8A, geometrical defects at the surfaces 8A, and partially melted and adhered powder 8B can be seen.

Some small-scale porosity defects can be observed, Figure 8A. Geometrical defects at the edge of the structure can be seen, although these are on the magnitude of 100 microns. Even after polishing, numerous spherical particulates can be seen at the edges of the geometry. This powder has partially melted into the surface, Figure 8B, due to the high energy density at the edges present with the contour scanning strategy used [43].

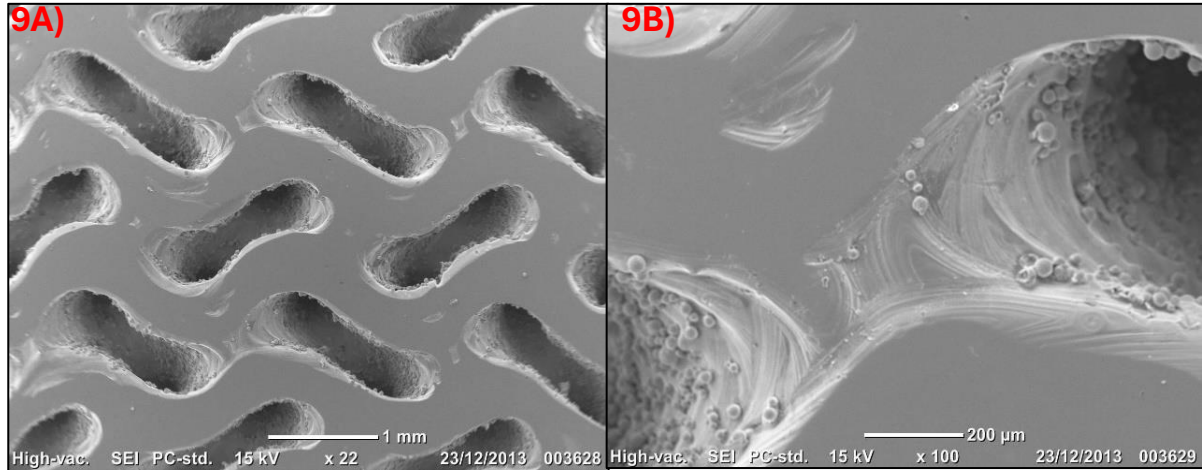


Figure 9 -Target Sheet Gyroid SEM Images. Geometrical defects 9A, and partially melted and adhered powder can be seen, 9B. Also, the lines left from melting and cooling, 9B, infer the presence of residual stresses from the rapid cooling times present in LPBF.

### 5.5.2 Alicona Optical microscope imagery

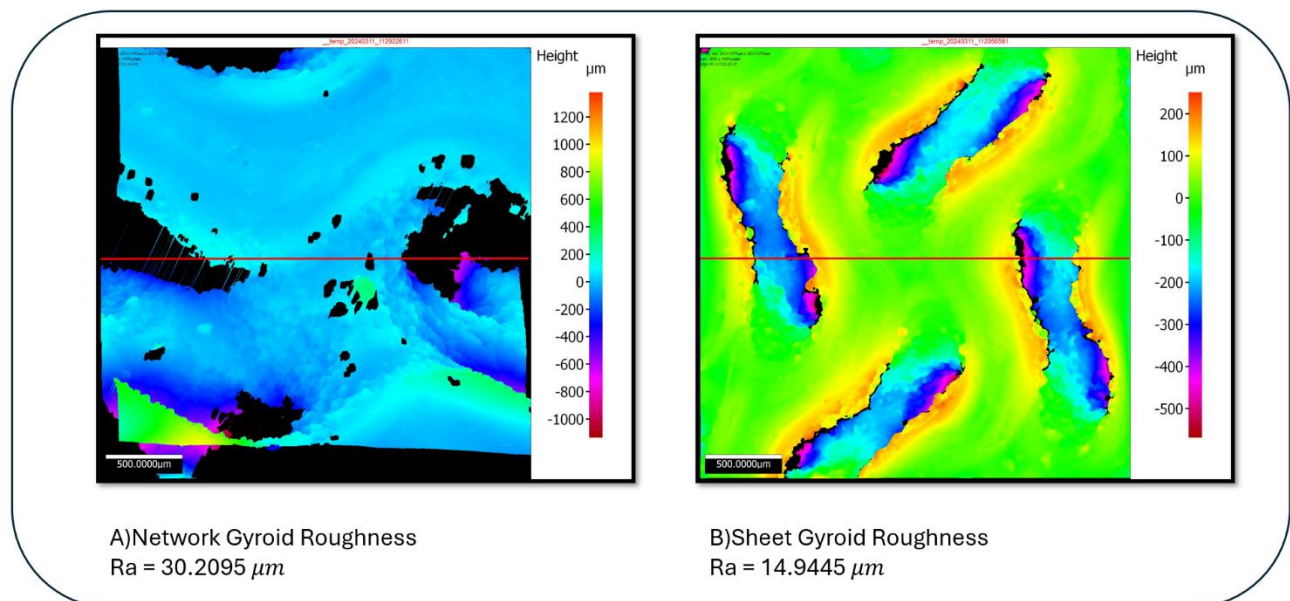


Figure 10- Alicona Contrast Images of upper surface of the two target gyroid lattices. The presence of significant balling on the internal surfaces can be seen in both lattices. Mean Surface roughness was consistent with the size range of the powder used, as the adhered powder dominates the peaks and valleys of the LPBF surface.

The roughness measurement of the sheet gyroid is much lower as the profile travels across the upper surface, which being the final layer in the build direction, has little adhered powder, and hence reduced surface roughness. This is due to the upper surface being in contact with less powder during printing. The network gyroid profile is majorly centred on the internal surface, and hence the roughness corresponds with the median partical size (30 Microns), as the internal surfaces have lots of adhered powder.

## 6 Discussion

### 6.1 Neural Networks, pre-training, and the effects of training iteration 2

The SNN offers a reasonable solution, although there is a clear advantage to the use of DNN architectures. What can be inferred from this is that the PTSP is a very complex function, which requires a more complex architecture to approximate [10]. This complexity arises from the multi-physics of LPBF that interact to form the phenomena of the PTSP, such as the melt pool, plateau-Rayleigh instability, and Marangoni flow [44]

Overall, the GLWPT has a detrimental effect on the accuracy of the PTSP approximation. This is due to the complexity of the method leading to overfitting. Even though the initial weights are identical to SAE, the layer-by-layer training identifies overly complex features that are only present in the training data. Inhibiting its ability to generalise to new data. Also, divergence is observed between the accuracy of the training data and the validation data, which is a clear sign of overfitting [45]. GLWPT requires a much larger data set to avoid this issue.

Overall, stacked autoencoder pre-training proved to be the more suitable pre-training method and improved consistency between different training runs. The SAE was the best NN for the network gyroids and was marginally outperformed by the RWB for the sheet gyroids. This method does not cause overfitting and provides a good initial 'guess' for the weights and biases for a small data set. Further work should investigate the optimal DNN architecture, for this strategy.

The approximation of the PTSP is enhanced using a broader data set [10]. Iteration 2 reduces the RMSE of almost all networks, only increasing RMSE on network gyroid GLWPT which is inherently unstable on small data sets. This improvement can be attributed to the interpolation between data points made by the NN's [45]. If a given validation data point in the high dimensional space lies 'between' two training data set points, the proximity of the training data points improves the quality of the validation point prediction. Including a better distribution of energy density improves this proximity. This enhanced proximity in the high dimensional space enables a more accurate extrapolation of the PTSP to predict the target lattice properties, which had design and process parameters not seen in the training data. By using the energy density to simplify the process parameter space the supplementary lattices could effectively reduce the high dimensional distance between the training and validation lattice data [24] And improve the approximation of the PTSP. This also demonstrates the suitability of the volumetric energy density as an approximation of the process parameter space. The process maps in Appendix B demonstrate a 2-dimensional slice of this higher process and design parameter space. The contours form rings around training data, thus more data points improve the approximated solution.

However, to enhance the work done in this study and improve the PTSP approximation for TPMS lattices, a much larger data set on the order of hundreds of lattices should be gathered [45] And further work should be done to include the additional parameters that influence the PTSP. Potentially making use of physics informed neural networks to incorporate the physics of the PTSP[46][47]. The effects of the additional parameters are most easily demonstrated with the target lattices. The implementation of Iteration 2 data significantly improves the accuracy of the target lattice predictions, which were manufactured on the same build plate as the supplementary lattices. Therefore, additional PTSP influencing parameters were kept constant across supplementary and target lattices. This leads to a 'micro-trend' within these lattices that is identified in the NN training and improves the predictions in Iteration 2. This is a common trend identified with ANN solutions to the PTSP[10], as approximations to the PTSP are often only valid for the study itself. Showcasing the presence of factors influential to the PTSP, that were not included in this work.

### 6.2 Micro-trends

Some potential factors that have been proposed for the creation of these micro-trends and are not included in this work are, the powder size distribution, which can lead to variations in the packing density of certain parts of the powder bed, in turn leading to porosity variation [48]. The scanning strategy of the laser[43], laser spot size[49], beam profile [50] , which can affect the microstructure, and gas flow field, which can affect the melt pool behaviour [51].

### 6.3 Differences in the PTSP relationship of sheet and network gyroids

A key observation within this work was that despite the similar sizes of the data sets, there was significantly reduced RMSE for all network gyroid NN's, and larger normalised errors for the sheet gyroid validation points. This infers that the PTSP relationship is more consistent for the network gyroids than the sheet gyroids, therefore sheet gyroids are more prone to variation. The target property predictions were only similar for both lattice types due to the micro-trend in the supplementary data.

As the sheet gyroid is a subtraction of two different network gyroid phases, the thickness of each curved wall is significantly smaller. Reaching wall thicknesses of ~250 microns in the target sheet gyroid (Figure 9B). [52] observed thermal instability in walls between 200-300 microns. Thin walls can lead to a greater sensitivity to dynamic behaviour of the melt pool [53], as the wall thickness to melt pool ratio is significantly smaller. Therefore, any geometrical deviations/defects caused by the dynamic behaviour of the melt pool (Spatters/denudation) [49] are relatively larger so have greater influence on the mechanical properties, than in the thicker walls of the network gyroid. Leading to the increased NN error. Further work should aim to identify changes in the resulting microstructure, as walls become thinner [43].

As the deformation mechanisms directly affect the mechanical properties [36], they can affect the PTSP for the two gyroid types. Defects caused by the dynamism of the melt pool, such as small-scale porosities, can lead to stress concentrations [54], which influence the YM and YS of the lattice (Elastic deformation region properties). Therefore, when all the layers of the sheet gyroid are compressed simultaneously in its elastic deformation, if the number of defects in each layer remains relatively constant [55], there is a larger number of defects adding variability in the measurement of the mechanical properties. Whereas network gyroids experience more local deformation in the first layer during elastic compression, which leads to less influence of defects. Therefore, there is a larger proportion of 'noise' in the measurement of the elastic mechanical properties for sheet gyroids than for network gyroids. Which explains the increased error in PTSP approximation on a similar data set size.

The different deformation mechanisms also account for the different mechanical properties observed. Sheet gyroids can achieve a higher yield strain of 11-15% as they undergo simultaneous layer collapse typical of bending dominated lattices [33]. Meaning that the strain energy is distributed across the entire lattice, and accounts for the larger YM and YS observed on a sheet gyroids [7], even with lower relative densities. The network gyroids experience layer by layer collapse [4], meaning that yield occurs at a lower strain, 6-8%, as the first layer experiences a greater concentration of strain energy and localised strain [32]. The regions of strain hardening/densification on Figure 7 showcase this deformation mechanism that is typical of stretch dominated lattices [37]. The strain energy can be calculated as the area under the stress strain graph, the decreasing area under the climb and peak regions for each subsequent layer collapse demonstrates the decreasing strain energy released during subsequent layer collapse [33]. Not all the strain energy is stored in the upper layer, but it contains a larger proportion of the distribution. Layer-by-layer collapse is advantageous for energy absorption applications [56].

Within the data from literature, there are a variety of strain rates from  $0.00033 \text{ s}^{-1}$  to  $0.01 \text{ s}^{-1}$ . Although these are within the range specified by the ISO 13314–2011, some approach much more quasistatic conditions, which has been shown to alter the recorded mechanical properties of bulk titanium alloy [57]. Incorporating the previous analysis of the strain energy distribution, deformation modes and the assumed equal distribution of defects in each layer. The increased variability during elastic deformation of the sheet gyroids could make them more sensitive to the varying strain rates used. Further work should be done on the dynamic loading of sheet gyroid lattices to investigate this hypothesis.

### 6.4 Differences observed between modulus and yield strength

The YM predictions had a greater error than the YS in all NN's. This highlights the greater complexity in the PTSP relationship for the YM. The PTSP is responsible for the distribution of defects within the lattice and the microstructure of the material, such as quality of fusion and grain structure, which can impact the elastic properties [10]. As there have been further parameters identified in the PTSP relationship, it can be reasoned that; as YS demonstrates consistently reduced percentage errors across the validation and target lattices, the

PTSP parameters included in this work are the primary factors influencing the YS. And the YM has variation associated with other factors, such as those attributed to the creation of micro trends.

### 6.5 ANN Limitations

A limitation to this method of function fitting NN to the PTSP, is that when targeting specific mechanical properties, the NN does not consider the phenomena which may not significantly affect the mechanical properties under its consideration. This led to the significant adhesion of powder observed on the surface of the target lattices, Figures 8, 9 and 10. Balling can be caused by the plateau-Rayleigh instability [44], however in this case as there was adequate fusion between layers, the mechanism behind the surface adhered powder was attributed to Marangoni flow. Where the low surface tension powder is attracted to the high surface tension of the melt pool [58]. The powder that has been drawn in is then partially melted. As it is half melted into the surface, it is difficult to remove from the internal surfaces with ultrasonic bath cleaning. Therefore, verification of surface quality should be conducted. This could be accomplished with in process monitoring and the use of convolutional NN (CNN) to identify at which process parameters this adhesion is caused, and to better understand the underlying mechanism [59].

## 7 Conclusions

ANN and pre training strategies with a small data set gathered from literature were used to predict and target the mechanical properties of TPMS sheet and network gyroid structures manufactured via LPBF. This was achieved by incorporating process and design parameters as inputs to the ANN, which output the mechanical properties of modulus and yield strength. Two target lattices were designed that had targeted mechanical properties pertaining to human bone, using process and design parameters supplied by NN's. There were also other supplementary lattices designed, fabricated, and tested to supplement the data from literature by filling in the energy density gaps in the data set.

- Of the pre-training strategies used, Stacked autoencoder outperformed the greedy layer wise method, and was the best performing NN for the network gyroid data set. Whilst also improving the prediction of target properties, achieving 8.76% accuracy for the YS, 31.8 % accuracy for YM.
- The network gyroid NN's were more accurate than the sheet gyroid NN's, with a similar data set size and identical training. Inferring the conclusion that the PTSP relationship for the network gyroids is simpler than for the sheet gyroids. This is attributed to the geometrical differences between the lattices, namely wall thickness. And the different deformation mechanisms.
- YS is more dependent on the parameters used in this study, whereas YM has more variation associated with the wider PTSP factors. DNN was able to achieve a yield strength prediction accuracy of 3.51 % for the target sheet gyroid, and 8.76 % accuracy for the target network gyroid.
- Sheet gyroids have larger YM and higher YS than network gyroids, for lower relative densities. They also had different deformation mechanisms, which make the network gyroid more suitable for energy absorption applications.
- TPMS gyroids achieved YM within the range for human bone, highlighting the suitability of this lattice structure to avoid stress shielding in implants.
- This method has limitations in the surface quality of the targeted lattices, there should be additional work conducted to ensure that the surface of the fabricated lattice is of the required standard. This could be achieved via post processing, or implementation of CNN to monitor the build in real time.
- The use of ANN in approximating the PTSP is severely limited by the size of the data set available in LPBF of TPMS lattices.
- Generalisation of the NN solution is challenging due to PTSP factors not kept constant across studies, which lead to 'micro-trends' within each study. Further work should aim to explore these factors, perhaps with an understanding of the physics/melt pool phenomena offered by physics informed NN or CNN.

## 8 Appendices

### 8.1 Appendix A: NN Training Data

Table 9-Iteration 2 data set

Layer Thickness (mm)	Laser Power(W)	Laser Scan Speed(mm/s)	Laser Hatch Spacing(mm)	Unit Cell Size(mm)	Designed Relative Density (%)	Youngs modulus (Mpa)	Yield Strength (Mpa)	Sheet or Network Gyroid	Source
0.03	275	1100	0.11	3	22.5	3437	126	sheet	[6]
0.03	275	1100	0.11	3	37.5	6731	266.2	sheet	[6]
0.03	275	1100	0.11	3	52.5	8559	423.6	sheet	[6]
0.03	275	1100	0.11	3	20	1453	61.9	net	[6]
0.03	275	1100	0.11	3	25	2219.9	88.9	net	[6]
0.03	275	1100	0.11	3	30	3088.8	115.2	net	[6]
0.03	200	1000	0.1	2	60	21700	762.7	sheet	[7]
0.03	200	1000	0.1	2	50	15300	608	sheet	[7]
0.03	200	1000	0.1	2	40	8800	476.3	sheet	[7]
0.03	240	240	0.05	1.5	30	5370	36.71	sheet	[13]
0.03	240	240	0.05	1.5	30	5460	33.49	sheet	[13]
0.03	240	240	0.05	1.5	30	5690	33.66	sheet	[13]
0.05	280	700	0.12	4	5.03	115.5	3.8	net	[60]
0.05	280	700	0.12	4	10.07	505.1	15.2	net	[60]
0.05	280	700	0.12	4	14.96	1052.3	27.2	net	[60]
0.05	280	700	0.12	4	20.01	1718	44.6	net	[60]
0.05	280	700	0.12	4	25.07	2490.4	67.1	net	[60]
0.05	280	700	0.12	4	30.04	3142.1	88.8	net	[60]
0.03	80	500	0.08	4	11.6	1641	47.3	sheet	[54]
0.03	80	500	0.08	4	14.5	1809	53.6	sheet	[54]
0.03	80	500	0.08	4	17.4	2038	78.8	sheet	[54]
0.03	80	500	0.08	4	23.1	2864	124.9	sheet	[54]
0.03	125	2800	0.05	4	17.9	5300	77.5	sheet	[61]
0.03	125	2800	0.05	4	35.9	14700	145.1	sheet	[61]
0.03	125	2800	0.05	6	11.9	3000	39.5	sheet	[61]
0.03	125	2800	0.05	6	23.6	6800	83.4	sheet	[61]
0.03	125	2800	0.05	6	46.1	13900	139.1	sheet	[61]
0.03	145	1000	0.05	6	11.9	3400	42.1	sheet	[61]
0.03	145	1000	0.05	6	46.1	16900	236	sheet	[61]
0.03	170	1250	0.06	4.5	5	134.7	5.2	net	[33]
0.03	170	1250	0.06	4.5	7.5	335.6	11.9	net	[33]
0.03	170	1250	0.06	4.5	10	601.9	20.9	net	[33]
0.03	170	1250	0.06	4.5	12.5	838.6	28.8	net	[33]
0.03	170	1250	0.06	4.5	15	1131.1	41	net	[33]
0.03	180	1250	0.03	5	20.41	1496.54	51.26	net	[62]
0.03	180	1250	0.03	5	4.6	135.63	5.32	net	[62]
0.03	180	1250	0.03	5	6.6	270.65	10.27	net	[62]
0.03	180	1250	0.03	5	8.6	400.72	16.25	net	[62]
0.03	180	1250	0.03	5	10.6	553.27	22.41	net	[62]
0.03	180	1250	0.03	5	12.6	764.23	31.15	net	[62]
0.03	275	1100	0.11	3	15	2208	97.1	sheet	[63]

0.03	275	1100	0.11	3	30	3569	181.1	sheet	[63]
0.03	275	1100	0.11	3	45	4658	356.7	sheet	[63]
0.03	200	1625	0.065	1	26.36	1950	48	net	[64]
0.03	200	1625	0.065	1	29.52	2450	77	net	[64]
0.03	300	240	0.07	1.7	34.5	1562	112	sheet	[65]
0.06	100	1250	0.06	1.5	30	1332	36.935	net	[66]
0.06	100	1250	0.06	1.5	25	806	28.54	net	[66]
0.06	100	1250	0.06	1.5	20	205	8.02	net	[66]
0.06	100	1250	0.06	1.5	15	134	4.43	net	[66]
0.03	170	1250	0.06	3	20	1743	52	sheet	[14]
0.03	170	1250	0.06	3	20	720.2	16	net	[14]
0.03	300	800	0.07	3	25	1070	128	sheet	[67]
0.03	300	800	0.07	2.5	28	1410	160	sheet	[67]
0.03	300	800	0.07	2	32	1420	166	sheet	[67]
0.03	280	1200	0.14	2.7	49.4	22000	186	sheet	[19]
0.03	240	1200	0.14	2.4	38.6	12600	119	sheet	[19]
0.03	200	1250	0.14	2.1	29.5	7600	75	sheet	[19]
0.03	150	1250	0.14	1.9	18.7	4800	51	sheet	[19]
0.03	100	385	0.12	2	27	2676	51.6	net	[1]
0.03	100	385	0.12	2.5	27	2170	44.9	net	[1]
0.03	100	385	0.12	3	27	1465	40.2	net	[1]
0.06	375	1200	0.19	2	25	1400	120	net	[68]
0.06	375	1200	0.19	2	25	1350	110	net	[68]
0.06	375	1200	0.19	2	25	1450	125	net	[68]
0.03	175	1250	0.1	2	20	1699	77.1	sheet	[36]
0.03	170	1250	0.06	5	15	806	47.6	net	[8]
0.03	100	1200	0.14	3	50	3211	97.97	sheet	[55]
0.03	150	1200	0.14	3	50	5224	171.31	sheet	[55]
0.03	200	1200	0.14	3	50	6172	218.399	sheet	[55]
0.03	250	1200	0.14	3	50	6072.69	226.57	sheet	[55]
0.03	300	1200	0.14	3	50	6331	228.54	sheet	[55]
0.03	330	1200	0.14	3	50	6364.89	235.55	sheet	[55]
0.03	360	1200	0.14	3	50	6366.89	234.48	sheet	[55]
0.03	280	1200	0.14	3	50	6168	226	sheet	[55]
0.03	120	1100	0.09	3	25	1516.5	65.15	net	(This Study)
0.03	200	570	0.09	3	25	1766.1	103.7	net	(This Study)
0.03	120	1100	0.09	3	35	2244.5	120.93	net	(This Study)
0.03	200	570	0.09	3	35	1559.5	79.3	net	(This Study)
0.03	220	580	0.09	3	30	2681.9	214.48	sheet	(This Study)
0.03	300	440	0.09	3	30	3663.4	285.4	sheet	(This Study)
0.03	220	580	0.09	3	45	3483.1	290.87	sheet	(This Study)
0.03	300	440	0.09	3	45	3852.8	516.67	sheet	(This Study)



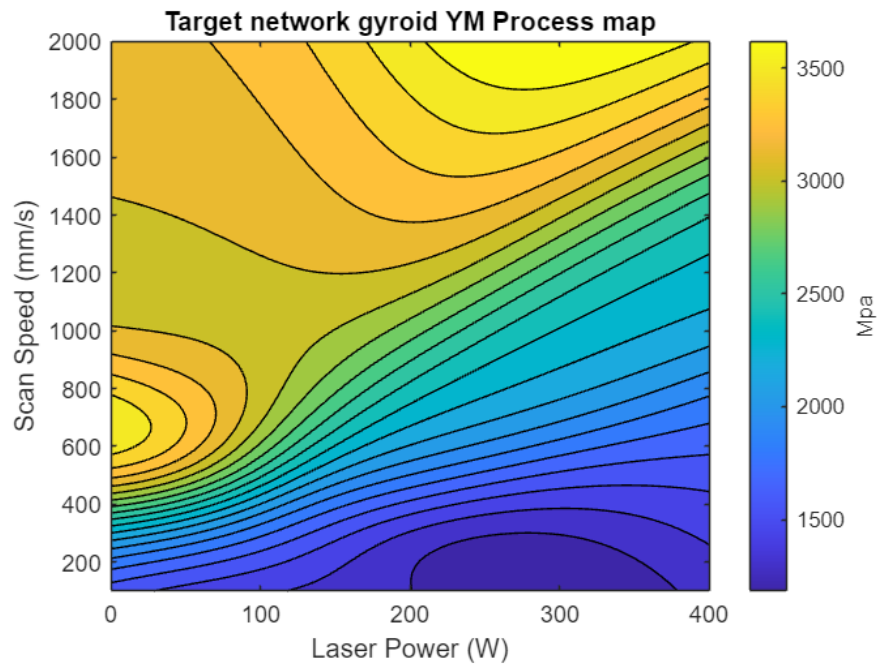
**8.2 Appendix B: Target lattice process maps**

Figure 11- Process map for Youngs modulus, target network gyroid. All other process and design parameters fixed according to table 2. From SAE Iteration 2.

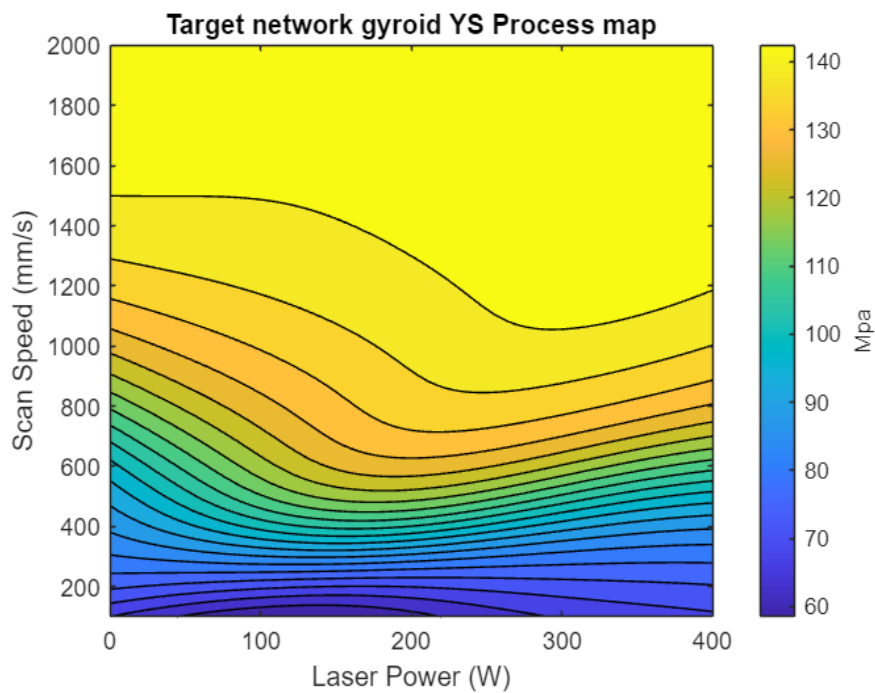


Figure 12- Process map for yield strength target network gyroid. All other process and design parameters fixed according to table 2. From SAE Iteration 2.

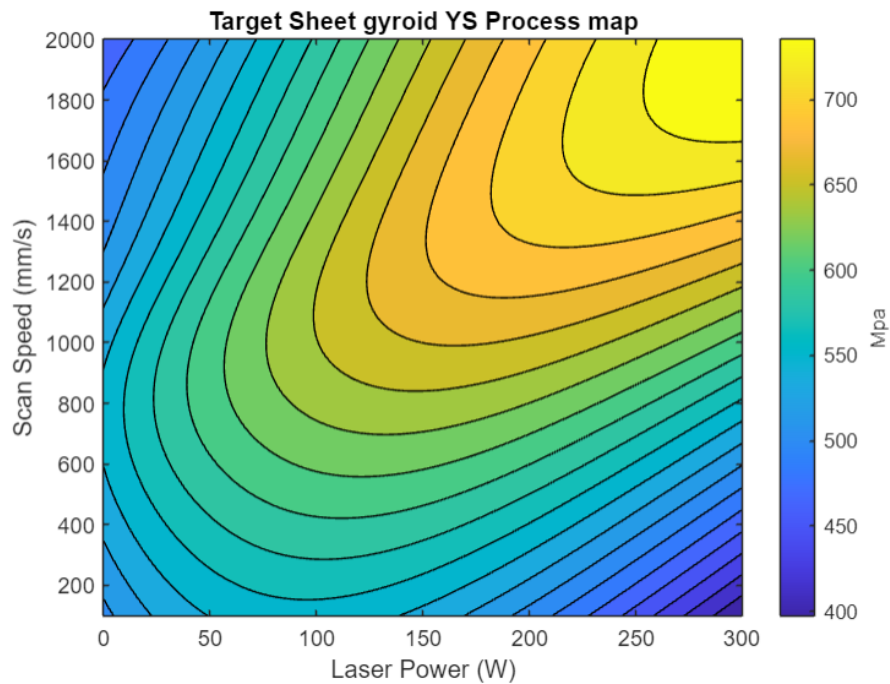


Figure 13- Process map for Youngs modulus, target sheet gyroid. All other process and design parameters fixed according to table 2. From RandWB Iteration 2.

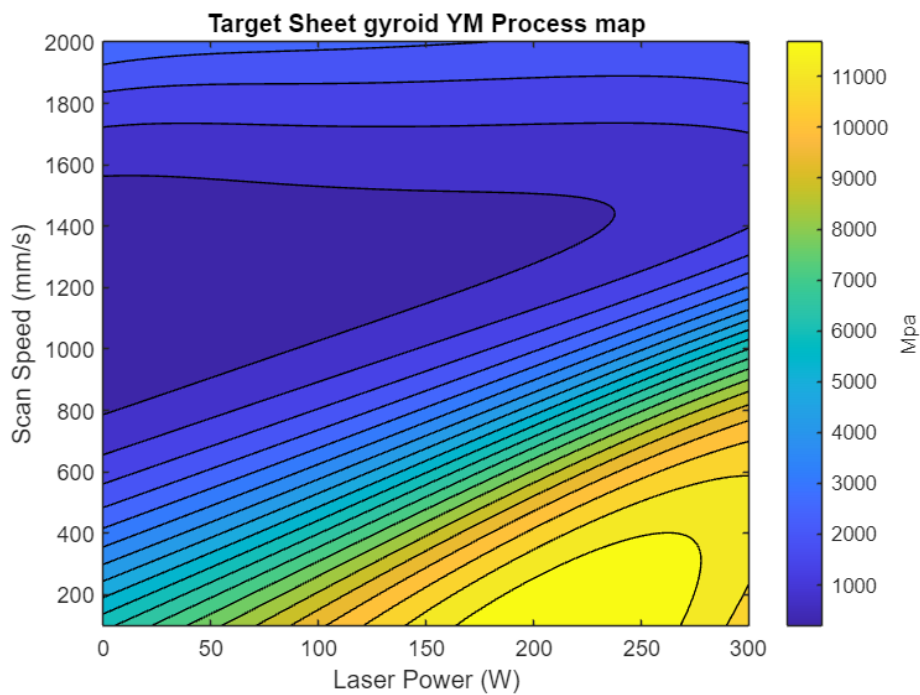
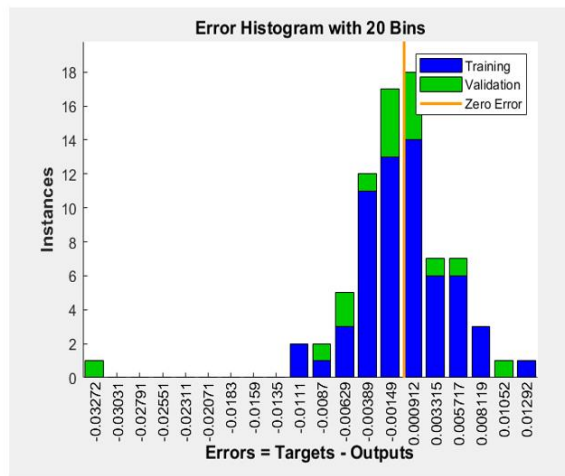
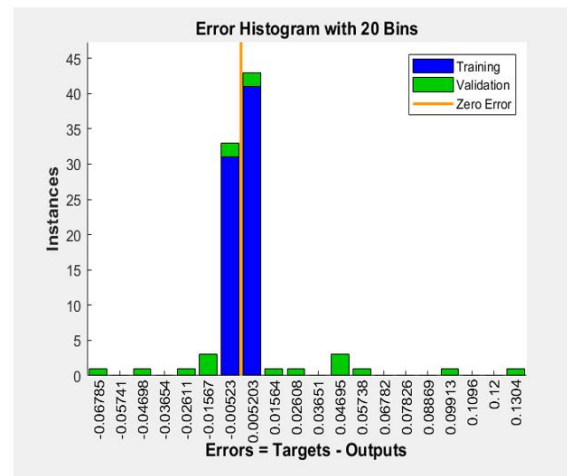


Figure 14- Process map for Youngs modulus, target network gyroid. All other process and design parameters fixed according to table 2. From RandWB Iteration 2.

### 8.3 Appendix C: Error histograms for Iteration 2 best networks



A) Error Histogram for SAENET



B) Error Histogram for RWBSHEET

Figure 15- Error histograms for SAE network and RandWB Sheet from iteration 2 of training. Corresponding to the validation plots of table 6. The more gaussian distribution seen in the network gyroid SAE demonstrates the reduced errors for the network gyroid, which are more centred around 0.

### 8.4 Appendix D: Iteration 1 best performing NN validation plots

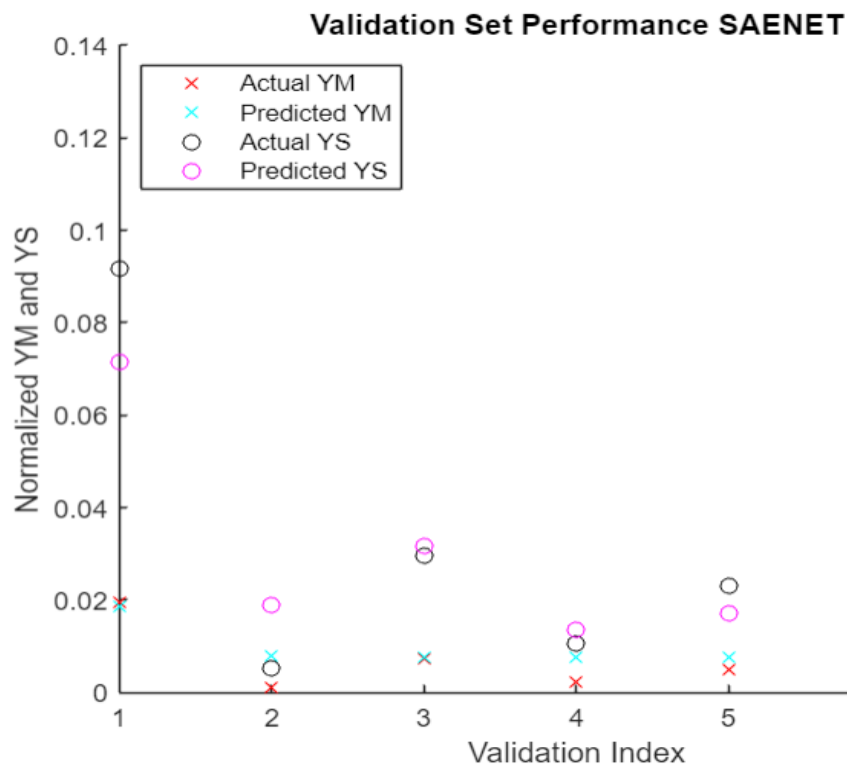


Figure 16- Iteration 1 SAENET validation accuracy

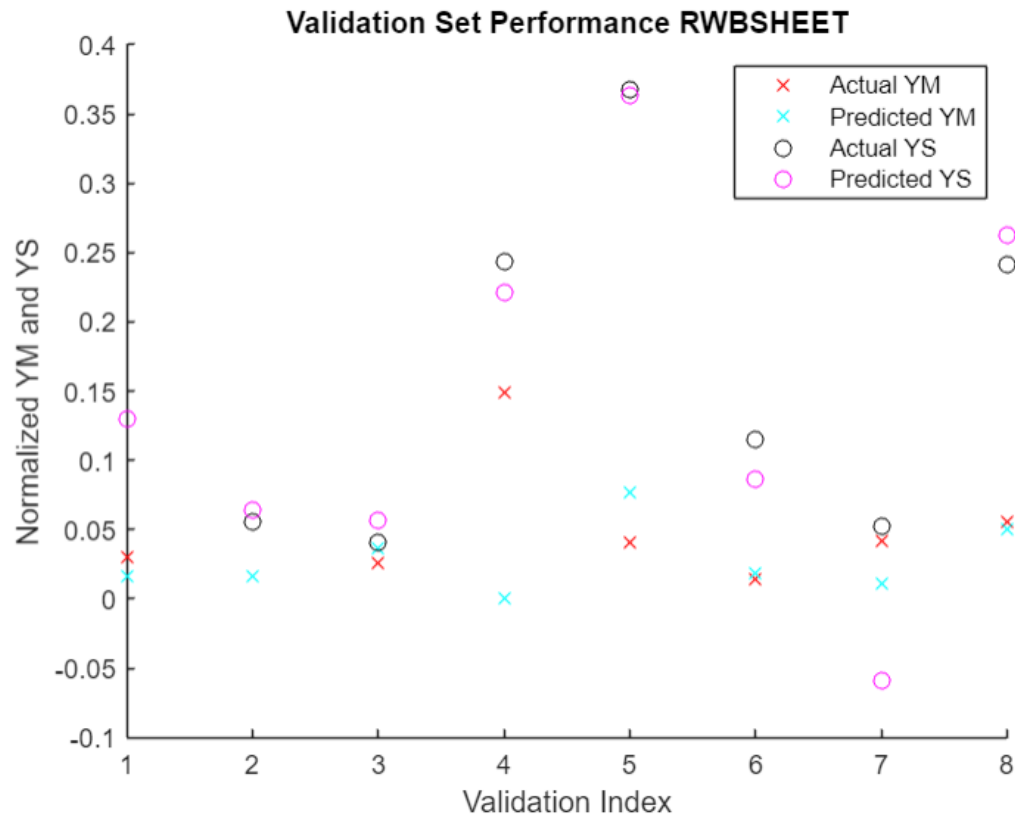


Figure 17- Iteration 1 RandWBSHEET validation accuracy

### 8.5 Appendix E: Supplementary lattice testing results

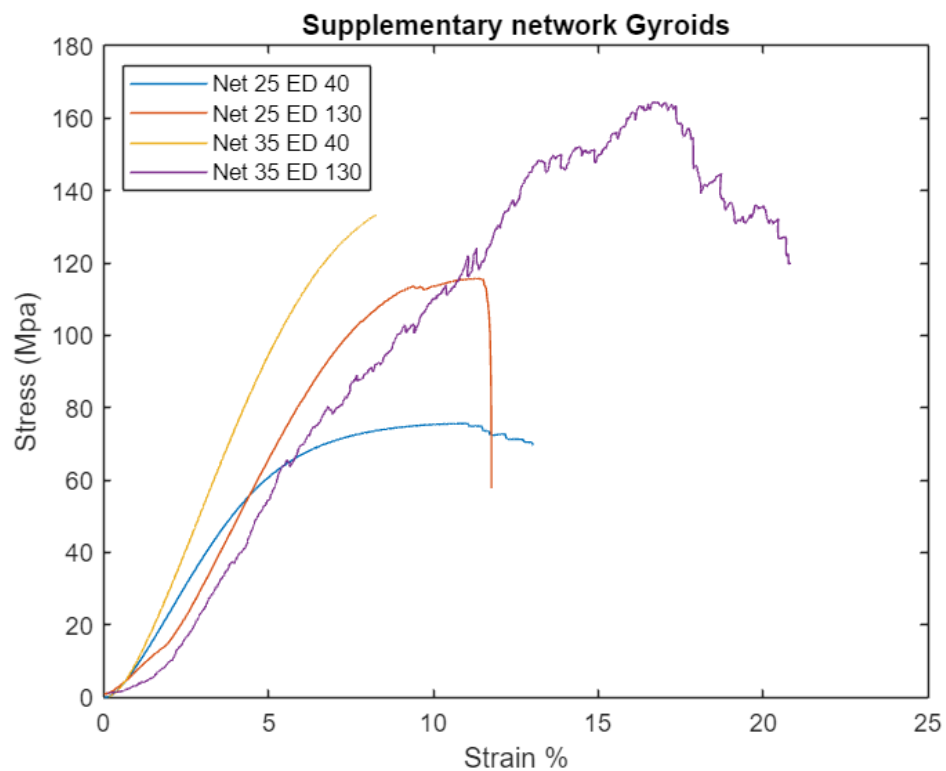


Figure 18- Supplementary network gyroid stress strain curves

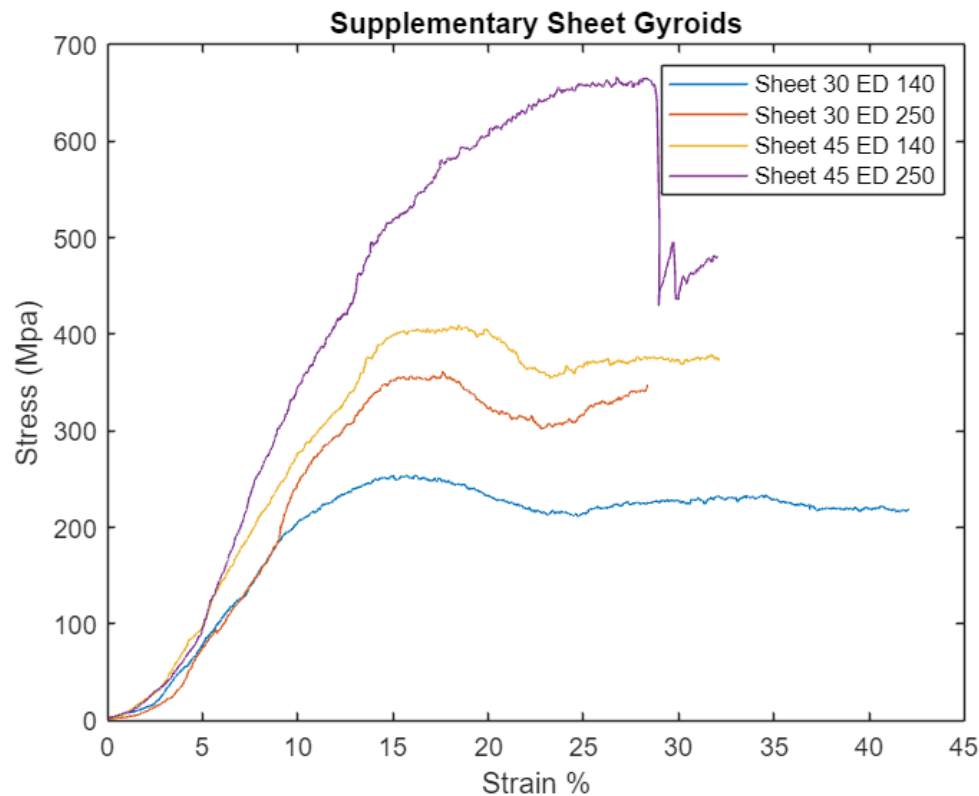


Figure 19- Supplementary sheet gyroid stress strain curves

## 9 Declaration of competing interest

The author declares that they have no known competing financial interests or personal relationships that could have appeared to influence the work reported in this paper.

## 10 Acknowledgements

I would like to thank Professor Khamis Essa for his invaluable guidance throughout this project, and Daniel Wilmot for his expertise in LPBF that was pivotal in this work.

## 11 References

- [1] A. Ataee, Y. Li, M. Brandt, and C. Wen, "Ultrahigh-strength titanium gyroid scaffolds manufactured by selective laser melting (SLM) for bone implant applications," *Acta Mater*, vol. 158, pp. 354–368, 2018, doi: <https://doi.org/10.1016/j.actamat.2018.08.005>.
- [2] Y. Zhang, G. S. Hong, D. Ye, K. Zhu, and J. Y. H. Fuh, "Extraction and evaluation of melt pool, plume and spatter information for powder-bed fusion AM process monitoring," *Mater Des*, vol. 156, pp. 458–469, 2018, doi: <https://doi.org/10.1016/j.matdes.2018.07.002>.
- [3] T. Maconachie *et al.*, "SLM lattice structures: Properties, performance, applications and challenges," *Materials and Design*, vol. 183, Elsevier Ltd, Dec. 05, 2019, doi: [10.1016/j.matdes.2019.108137](https://doi.org/10.1016/j.matdes.2019.108137).
- [4] M. F. Ashby, "The Properties of Foams and Lattices," *Philosophical Transactions: Mathematical, Physical and Engineering Sciences*, vol. 364, no. 1838, pp. 15–30, 2006, [Online]. Available: <http://www.jstor.org/stable/25190170>
- [5] S. A. Tyagi and M. Manjaiah, "Printability, post-processing and mechanical behaviour of sub-millimetre sized SS 17-4PH TPMS lattice structures," *Mater Today Commun*, vol. 38, p. 108267, 2024, doi: <https://doi.org/10.1016/j.mtcomm.2024.108267>.
- [6] Z. Luo *et al.*, "Finite element analysis of the mechanical properties of sheet- and skeleton-gyroid Ti6Al4V structures produced by laser powder bed fusion," *Thin-Walled Structures*, vol. 192, p. 111098, 2023, doi: <https://doi.org/10.1016/j.tws.2023.111098>.

- [7] N. Wang, G. K. Meenashisundaram, D. Kandilya, J. Y. H. Fuh, S. T. Dheen, and A. S. Kumar, "A biomechanical evaluation on Cubic, Octet, and TPMS gyroid Ti6Al4V lattice structures fabricated by selective laser melting and the effects of their debris on human osteoblast-like cells," *Biomaterials Advances*, vol. 137, p. 212829, 2022, doi: <https://doi.org/10.1016/j.bioadv.2022.212829>.
- [8] C. Yan, L. Hao, A. Hussein, Q. Wei, and Y. Shi, "Microstructural and surface modifications and hydroxyapatite coating of Ti-6Al-4V triply periodic minimal surface lattices fabricated by selective laser melting," *Materials Science and Engineering: C*, vol. 75, pp. 1515–1524, 2017, doi: <https://doi.org/10.1016/j.msec.2017.03.066>.
- [9] L. Meng *et al.*, "Machine Learning in Additive Manufacturing: A Review," *JOM*, vol. 72, no. 6, pp. 2363–2377, 2020, doi: [10.1007/s11837-020-04155-y](https://doi.org/10.1007/s11837-020-04155-y).
- [10] P. Wang, Y. Yang, and N. S. Moghaddam, "Process modeling in laser powder bed fusion towards defect detection and quality control via machine learning: The state-of-the-art and research challenges," *J Manuf Process*, vol. 73, pp. 961–984, 2022, doi: <https://doi.org/10.1016/j.jmapro.2021.11.037>.
- [11] J. Feng, J. Fu, X. Yao, and Y. He, "Triply periodic minimal surface (TPMS) porous structures: From multi-scale design, precise additive manufacturing to multidisciplinary applications," *International Journal of Extreme Manufacturing*, vol. 4, no. 2. IOP Publishing Ltd, Jun. 01, 2022. doi: [10.1088/2631-7990/ac5be6](https://doi.org/10.1088/2631-7990/ac5be6).
- [12] H. Hassanin, Y. Alkendi, M. Elsayed, K. Essa, and Y. Zweiri, "Controlling the Properties of Additively Manufactured Cellular Structures Using Machine Learning Approaches," *Adv Eng Mater*, vol. 22, no. 3, Mar. 2020, doi: [10.1002/adem.201901338](https://doi.org/10.1002/adem.201901338).
- [13] J. Ge *et al.*, "Microstructural features and compressive properties of SLM Ti6Al4V lattice structures," *Surf Coat Technol*, vol. 403, p. 126419, 2020, doi: <https://doi.org/10.1016/j.surfcoat.2020.126419>.
- [14] H. Zhou, M. Zhao, Z. Ma, D. Z. Zhang, and G. Fu, "Sheet and network based functionally graded lattice structures manufactured by selective laser melting: Design, mechanical properties, and simulation," *Int J Mech Sci*, vol. 175, p. 105480, 2020, doi: <https://doi.org/10.1016/j.ijmecsci.2020.105480>.
- [15] G. K. Sarkon, B. Safaei, M. S. Kenevisi, S. Arman, and Q. Zeeshan, "State-of-the-Art Review of Machine Learning Applications in Additive Manufacturing; from Design to Manufacturing and Property Control," *Archives of Computational Methods in Engineering*, vol. 29, no. 7, pp. 5663–5721, 2022, doi: [10.1007/s11831-022-09786-9](https://doi.org/10.1007/s11831-022-09786-9).
- [16] S. Feng, H. Zhou, and H. Dong, "Using deep neural network with small dataset to predict material defects," *Mater Des*, vol. 162, pp. 300–310, 2019, doi: <https://doi.org/10.1016/j.matdes.2018.11.060>.
- [17] T. L. Passafaro *et al.*, "Would large dataset sample size unveil the potential of deep neural networks for improved genome-enabled prediction of complex traits? The case for body weight in broilers," *BMC Genomics*, vol. 21, no. 1, p. 771, 2020, doi: [10.1186/s12864-020-07181-x](https://doi.org/10.1186/s12864-020-07181-x).
- [18] S. A. Tyagi and M. M., "Additive manufacturing of titanium-based lattice structures for medical applications – A review," *Bioprinting*, vol. 30, p. e00267, 2023, doi: <https://doi.org/10.1016/j.bprint.2023.e00267>.
- [19] A. Timercan, P. Terriault, and V. Brailovski, "Axial tension/compression and torsional loading of diamond and gyroid lattice structures for biomedical implants: Simulation and experiment," *Mater Des*, vol. 225, p. 111585, 2023, doi: <https://doi.org/10.1016/j.matdes.2022.111585>.
- [20] R. Santiago *et al.*, "Modelling and optimisation of TPMS-based lattices subjected to high strain-rate impact loadings," *Int J Impact Eng*, vol. 177, p. 104592, 2023, doi: <https://doi.org/10.1016/j.ijimpeng.2023.104592>.
- [21] F. Distefano, S. Pasta, and G. Epasto, "Titanium Lattice Structures Produced via Additive Manufacturing for a Bone Scaffold: A Review," *Journal of Functional Biomaterials*, vol. 14, no. 3. MDPI, Mar. 01, 2023. doi: [10.3390/jfb14030125](https://doi.org/10.3390/jfb14030125).
- [22] Y. W. Luo *et al.*, "Pore-affected fatigue life scattering and prediction of additively manufactured Inconel 718: An investigation based on miniature specimen testing and machine learning approach," *Materials Science and Engineering: A*, vol. 802, p. 140693, 2021, doi: <https://doi.org/10.1016/j.msea.2020.140693>.
- [23] W. Muhammad, A. P. Brahme, O. Ibragimova, J. Kang, and K. Inal, "A machine learning framework to predict local strain distribution and the evolution of plastic anisotropy & fracture in additively manufactured alloys," *Int J Plast*, vol. 136, p. 102867, 2021, doi: <https://doi.org/10.1016/j.ijplas.2020.102867>.
- [24] K. G. Prashanth, S. Scudino, T. Maity, J. Das, and J. Eckert, "Is the energy density a reliable parameter for materials synthesis by selective laser melting?," *Mater Res Lett*, vol. 5, no. 6, pp. 386–390, Nov. 2017, doi: [10.1080/21663831.2017.1299808](https://doi.org/10.1080/21663831.2017.1299808).
- [25] Alistair Jones, "TPMS Designer." Accessed: May 06, 2024. [Online]. Available: <https://uk.mathworks.com/matlabcentral/fileexchange/78838-tpms-designer>
- [26] A. Gaikwad *et al.*, "Multi Phenomena Melt Pool Sensor Data Fusion for Enhanced Process Monitoring of Laser Powder Bed Fusion Additive Manufacturing," *Mater Des*, vol. 221, p. 110919, Jul. 2022, doi: [10.1016/j.matdes.2022.110919](https://doi.org/10.1016/j.matdes.2022.110919).
- [27] O. Isaac Abiodun, A. Jantan, A. Esther Omolara, K. Victoria Dada, N. AbdElatif Mohamed, and H. Arshad, "State-of-the-art in artificial neural network applications: A survey," *Heliyon*, vol. 4, p. 938, 2018, doi: [10.1016/j.heliyon.2018](https://doi.org/10.1016/j.heliyon.2018).

- [28] W.-K. Hong, "Understanding artificial neural networks: analogy to the biological neuron model," in *Artificial Intelligence-Based Design of Reinforced Concrete Structures*, Elsevier, 2023, pp. 7–13. doi: 10.1016/b978-0-443-15252-8.00003-0.
- [29] "Trainrp Matlab Documentation." Accessed: May 02, 2024. [Online]. Available: [https://uk.mathworks.com/help/deeplearning/ref/trainrp.html#responsive\\_offcanvas](https://uk.mathworks.com/help/deeplearning/ref/trainrp.html#responsive_offcanvas)
- [30] X. Yuan, C. Ou, Y. Wang, C. Yang, and W. Gui, "A novel semi-supervised pre-training strategy for deep networks and its application for quality variable prediction in industrial processes," *Chem Eng Sci*, vol. 217, p. 115509, 2020, doi: <https://doi.org/10.1016/j.ces.2020.115509>.
- [31] M. McGregor, S. Patel, S. McLachlin, and Mihaela Vlasea, "Architectural bone parameters and the relationship to titanium lattice design for powder bed fusion additive manufacturing," *Addit Manuf*, vol. 47, p. 102273, 2021, doi: <https://doi.org/10.1016/j.addma.2021.102273>.
- [32] H. Zhong, T. Song, C. Li, R. Das, J. Gu, and M. Qian, "The Gibson-Ashby model for additively manufactured metal lattice materials: Its theoretical basis, limitations and new insights from remedies," *Curr Opin Solid State Mater Sci*, vol. 27, no. 3, p. 101081, 2023, doi: <https://doi.org/10.1016/j.cossms.2023.101081>.
- [33] L. Yang, C. Yan, C. Han, P. Chen, S. Yang, and Y. Shi, "Mechanical response of a triply periodic minimal surface cellular structures manufactured by selective laser melting," *Int J Mech Sci*, vol. 148, pp. 149–157, 2018, doi: <https://doi.org/10.1016/j.ijmecsci.2018.08.039>.
- [34] M. Shen *et al.*, "Mechanical properties of 3D printed ceramic cellular materials with triply periodic minimal surface architectures," *J Eur Ceram Soc*, vol. 41, no. 2, pp. 1481–1489, 2021, doi: <https://doi.org/10.1016/j.jeurceramsoc.2020.09.062>.
- [35] Y. Liang *et al.*, "Energy Absorption and Deformation Behavior of 3D Printed Triply Periodic Minimal Surface Stainless Steel Cellular Structures under Compression," *Steel Res Int*, vol. 92, no. 3, Mar. 2021, doi: 10.1002/srin.202000411.
- [36] M. Zhao, D. Z. Zhang, F. Liu, Z. Li, Z. Ma, and Z. Ren, "Mechanical and energy absorption characteristics of additively manufactured functionally graded sheet lattice structures with minimal surfaces," *Int J Mech Sci*, vol. 167, p. 105262, 2020, doi: <https://doi.org/10.1016/j.ijmecsci.2019.105262>.
- [37] T. Maconachie *et al.*, "SLM lattice structures: Properties, performance, applications and challenges," *Materials and Design*, vol. 183. Elsevier Ltd, Dec. 05, 2019. doi: 10.1016/j.matdes.2019.108137.
- [38] D. Khrapov *et al.*, "Trapped powder removal from sheet-based porous structures based on triply periodic minimal surfaces fabricated by electron beam powder bed fusion," *Materials Science and Engineering: A*, vol. 862, p. 144479, 2023, doi: <https://doi.org/10.1016/j.msea.2022.144479>.
- [39] M. Boutaous, X. Liu, D. A. Siginer, and S. Xin, "Balling phenomenon in metallic laser based 3D printing process," *International Journal of Thermal Sciences*, vol. 167, p. 107011, 2021, doi: <https://doi.org/10.1016/j.ijthermalsci.2021.107011>.
- [40] V. Lindström, G. Lupo, J. Yang, V. Turlo, and C. Leinenbach, "A simple scaling model for balling defect formation during laser powder bed fusion," *Addit Manuf*, vol. 63, p. 103431, 2023, doi: <https://doi.org/10.1016/j.addma.2023.103431>.
- [41] J. Tang *et al.*, "Impacts of residual 3D printing metal powders on immunological response and bone regeneration: an in vivo study," *J Mater Sci Mater Med*, vol. 34, no. 6, Jun. 2023, doi: 10.1007/s10856-023-06727-1.
- [42] J. C. Tang *et al.*, "Immunological response triggered by metallic 3D printing powders," *Addit Manuf*, vol. 35, p. 101392, 2020, doi: <https://doi.org/10.1016/j.addma.2020.101392>.
- [43] H. Jia, H. Sun, H. Wang, Y. Wu, and H. Wang, "Scanning strategy in selective laser melting (SLM): a review," *The International Journal of Advanced Manufacturing Technology*, vol. 113, no. 9, pp. 2413–2435, 2021, doi: 10.1007/s00170-021-06810-3.
- [44] J. Wang, R. Zhu, Y. Liu, and L. Zhang, "Understanding melt pool characteristics in laser powder bed fusion: An overview of single- and multi-track melt pools for process optimization," *Advanced Powder Materials*, vol. 2, no. 4, p. 100137, 2023, doi: <https://doi.org/10.1016/j.apmate.2023.100137>.
- [45] X. Qi, G. Chen, Y. Li, X. Cheng, and C. Li, "Applying Neural-Network-Based Machine Learning to Additive Manufacturing: Current Applications, Challenges, and Future Perspectives," *Engineering*, vol. 5, no. 4, pp. 721–729, 2019, doi: <https://doi.org/10.1016/j.eng.2019.04.012>.
- [46] K. Shi, D. Gu, H. Liu, Y. Chen, and K. Lin, "Process-structure multi-objective inverse optimisation for additive manufacturing of lattice structures using a physics-enhanced data-driven method," *Virtual Phys Prototyp*, vol. 18, no. 1, p. e2266641, Dec. 2023, doi: 10.1080/17452759.2023.2266641.
- [47] Q. Zhu, Z. Liu, and J. Yan, "Machine learning for metal additive manufacturing: predicting temperature and melt pool fluid dynamics using physics-informed neural networks," *Comput Mech*, vol. 67, no. 2, pp. 619–635, 2021, doi: 10.1007/s00466-020-01952-9.
- [48] U. Habiba and R. J. Hebert, "Powder Spreading Mechanism in Laser Powder Bed Fusion Additive Manufacturing: Experiments and Computational Approach Using Discrete Element Method," *Materials*, vol. 16, no. 7, Apr. 2023, doi: 10.3390/ma16072824.



- [49] M. C. Sow *et al.*, "Influence of beam diameter on Laser Powder Bed Fusion (L-PBF) process," *Addit Manuf*, vol. 36, p. 101532, 2020, doi: <https://doi.org/10.1016/j.addma.2020.101532>.
- [50] W. Yuan, H. Chen, S. Li, Y. Heng, S. Yin, and Q. Wei, "Understanding of adopting flat-top laser in laser powder bed fusion processed Inconel 718 alloy: simulation of single-track scanning and experiment," *Journal of Materials Research and Technology*, vol. 16, pp. 1388–1401, 2022, doi: <https://doi.org/10.1016/j.jmrt.2021.12.077>.
- [51] Z. Liu *et al.*, "Flow field analysis for multilaser powder bed fusion and the influence of gas flow distribution on parts quality," *Rapid Prototyp J*, vol. 28, no. 9, pp. 1706–1716, Oct. 2022, doi: [10.1108/RPJ-12-2021-0351](https://doi.org/10.1108/RPJ-12-2021-0351).
- [52] J. Kranz, D. Herzog, and C. Emmelmann, "Design guidelines for laser additive manufacturing of lightweight structures in TiAl6V4," *J Laser Appl*, vol. 27, no. S1, p. S14001, Dec. 2014, doi: [10.2351/1.4885235](https://doi.org/10.2351/1.4885235).
- [53] D. Wang, S. Wu, Y. Bai, H. Lin, Y. Yang, and C. Song, "Characteristics of typical geometrical features shaped by selective laser melting," *J Laser Appl*, vol. 29, no. 2, p. 022007, Apr. 2017, doi: [10.2351/1.4980164](https://doi.org/10.2351/1.4980164).
- [54] Q. Sun, J. Sun, K. Guo, and L. Wang, "Compressive mechanical properties and energy absorption characteristics of SLM fabricated Ti6Al4V triply periodic minimal surface cellular structures," *Mechanics of Materials*, vol. 166, p. 104241, 2022, doi: <https://doi.org/10.1016/j.mechmat.2022.104241>.
- [55] A. du Plessis, N. Razavi, and F. Berto, "The effects of microporosity in struts of gyroid lattice structures produced by laser powder bed fusion," *Mater Des*, vol. 194, p. 108899, 2020, doi: <https://doi.org/10.1016/j.matdes.2020.108899>.
- [56] M. Mazur, M. Leary, M. McMillan, S. Sun, D. Shidid, and M. Brandt, "5 - Mechanical properties of Ti6Al4V and AlSi12Mg lattice structures manufactured by Selective Laser Melting (SLM)," in *Laser Additive Manufacturing*, M. Brandt, Ed., Woodhead Publishing, 2017, pp. 119–161. doi: <https://doi.org/10.1016/B978-0-08-100433-3.00005-1>.
- [57] W.-S. Lee and M.-T. Lin, "The effects of strain rate and temperature on the compressive deformation behaviour of Ti6Al4V alloy," *J Mater Process Technol*, vol. 71, no. 2, pp. 235–246, 1997, doi: [https://doi.org/10.1016/S0924-0136\(97\)00080-0](https://doi.org/10.1016/S0924-0136(97)00080-0).
- [58] B. Cox, M. Ghayoor, S. Pasebani, and J. Gess, "Tracking of Marangoni driven motion during laser powder bed fusion," *Powder Technol*, vol. 425, p. 118610, 2023, doi: <https://doi.org/10.1016/j.powtec.2023.118610>.
- [59] J. Qin *et al.*, "Research and application of machine learning for additive manufacturing," *Addit Manuf*, vol. 52, p. 102691, 2022, doi: <https://doi.org/10.1016/j.addma.2022.102691>.
- [60] J. Zhang, B. Song, L. Yang, R. Liu, L. Zhang, and Y. Shi, "Microstructure evolution and mechanical properties of TiB/Ti6Al4V gradient-material lattice structure fabricated by laser powder bed fusion," *Compos B Eng*, vol. 202, p. 108417, 2020, doi: <https://doi.org/10.1016/j.compositesb.2020.108417>.
- [61] C. N. Kelly *et al.*, "Fatigue behavior of As-built selective laser melted titanium scaffolds with sheet-based gyroid microarchitecture for bone tissue engineering," *Acta Biomater*, vol. 94, pp. 610–626, 2019, doi: <https://doi.org/10.1016/j.actbio.2019.05.046>.
- [62] X. Shi *et al.*, "Comparison of Compression Performance and Energy Absorption of Lattice Structures Fabricated by Selective Laser Melting," *Adv Eng Mater*, vol. 22, no. 11, p. 2000453, Nov. 2020, doi: <https://doi.org/10.1002/adem.202000453>.
- [63] X. Fan *et al.*, "Design, mechanical properties and energy absorption capability of graded-thickness triply periodic minimal surface structures fabricated by selective laser melting," *Int J Mech Sci*, vol. 204, p. 106586, 2021, doi: <https://doi.org/10.1016/j.ijmecsci.2021.106586>.
- [64] D. Mahmoud, K. S. Al-Rubaie, and M. A. Elbestawi, "The influence of selective laser melting defects on the fatigue properties of Ti6Al4V porosity graded gyroids for bone implants," *Int J Mech Sci*, vol. 193, p. 106180, 2021, doi: <https://doi.org/10.1016/j.ijmecsci.2020.106180>.
- [65] L. Liu, S. Wang, J. Liu, F. Deng, Z. Li, and Y. Hao, "Architectural design of Ti6Al4V scaffold controls the osteogenic volume and application area of the scaffold," *Journal of Materials Research and Technology*, vol. 9, no. 6, pp. 15849–15861, 2020, doi: <https://doi.org/10.1016/j.jmrt.2020.11.061>.
- [66] C. M. Suryawanshi, S. Sagar, R. Bhallamudi, and S. Mishra, "Effective design and mechanical response of Gyroid lattice scaffold for orthopedic implants," *Manuf Lett*, vol. 35, pp. 493–501, 2023, doi: <https://doi.org/10.1016/j.mfglet.2023.07.015>.
- [67] M. Ebrahimi, A. Kermanpur, and M. Kharaziha, "The effects of pore size and heat treatment on compression and corrosion behaviors of Ti-6Al-4V sheet-based gyroid implants fabricated by laser powder-bed fusion process," *Journal of Materials Research and Technology*, vol. 26, pp. 7707–7721, 2023, doi: <https://doi.org/10.1016/j.jmrt.2023.09.130>.
- [68] L. Yang *et al.*, "Fatigue properties of Ti-6Al-4V Gyroid graded lattice structures fabricated by laser powder bed fusion with lateral loading," *Addit Manuf*, vol. 46, p. 102214, 2021, doi: <https://doi.org/10.1016/j.addma.2021.102214>.